Calorimetry at a Future Linear Collider

Steven Green
of Emmanuel College

A dissertation submitted to the University of Cambridge
for the degree of Doctor of Philosophy

Abstract

This thesis describes the optimisation of the calorimeter design for collider experiments at the future Compact LInear Collider (CLIC) and the International Linear Collider (ILC). The detector design of these experiments is built around high-granularity Particle Flow Calorimetry that, in contrast to traditional calorimetry, uses the energy measurements for charged particles from the tracking detectors. This can only be realised if calorimetric energy deposits from charged particles can be separated from those of neutral particles. This is made possible with fine granularity calorimeters and sophisticated pattern recognition software, which is provided by the PandoraPFA algorithm. This thesis presents results on Particle Flow calorimetry performance for a number of detector configurations. To obtain these results a new calibration procedure was developed and applied to the detector simulation and reconstruction to ensure optimal performance was achieved for each detector configuration considered.

This thesis also describes the development of a software compensation technique that vastly improves the intrinsic energy resolution of a Particle Flow Calorimetry detector. This technique is implemented within the PandoraPFA framework and demonstrates the gains that can be made by fully exploiting the information provided by the fine granularity calorimeters envisaged at a future linear collider.

A study of the sensitivity of the CLIC experiment to anomalous gauge couplings that effect vector boson scattering processes is presented. These anomalous couplings provide insight into possible beyond standard model physics. This study, which utilises the excellent jet energy resolution from Particle Flow Calorimetry, was performed at centre-of-mass energies of 1.4 TeV and 3 TeV with integrated luminosities of 1.5ab^{-1}

and 2ab^{-1} respectively. The precision achievable at CLIC is shown to be approximately one to two orders of magnitude better than that currently offered by the LHC.

In addition, a study into various technology options for the CLIC vertex detector is described.

Declaration

This dissertation is the result of my own work, except where explicit reference is made to the work of others, and has not been submitted for another qualification to this or any other university. This dissertation does not exceed the word limit for the respective Degree Committee.

Steven Green

vii

Acknowledgements

Of the many people who deserve thanks, some are particularly prominent, such as my supervisor...

Contents

*"Writing in English is the most ingenious torture
ever devised for sins committed in previous lives."*
— James Joyce

Chapter 1

Energy Estimators

"There, sir! that is the perfection of vessels!"
    — Jules Verne, 1828–1905

1.1 Motivation

This section outlines a procedure for calibrating the Monte-Carlo (MC) response of the linear collider detector simulations with a focus on converting the detector response into accurate energy measurements, "energy estimators", for particles showering in the calorimeters. In the particle flow paradigm, all neutral particle energies are measured using the calorimeters, which makes accurate energy reconstruction crucial for determining detector performance. Additionally, comparisons of particle shower energy and charged particle track momenta govern the event reconstruction in PandoraPFA during the reclustering stage, which further emphasises the importance of reliable energy estimators.

The goal of a calorimeter is to measure the energy of particles that shower within it. Particle showers are a cascade of secondary particles that are produced as a high energy particle interacts with a dense material. The energy deposits produced by a showering particle in the calorimeter are referred to as hits. The number of hits created by a particle shower in a calorimeter depends upon the size and shape of the particle shower and the segmentation of the calorimeter. The energy of the showering particle, $E_{Cluster}$, is determined by grouping these energy deposits together into clusters and summing their

energy

$$E_{Cluster} = \sum_{ECal\ hits,\ i} E^i_{ECal} + \sum_{HCal\ hits,\ i} E^i_{HCal} \ , \qquad (1.1)$$

where E^i_{ECal} is the energy of ECal hit i and E^i_{HCal} is the energy HCal hit i. In this example, the energy deposits are assumed to be split across an ECal and a HCal, therefore, the sum runs over the hits in both calorimeters. This naive energy estimator will act as a starting point for the development of more sophisticated procedures aimed at improving the energy resolution.

The linear collider detector concepts employ highly-granular sampling calorimeters [1, 2]. These calorimeters are comprised of alternating layers of active and absorber materials [3]. The absorber layers initiate particle showers and propagate their growth, while the active layers produce a signal that is proportional to the energy deposited within them. The signal produced in the active layers is measured by sampling calorimeters and used to estimate the energy deposited in the absorber layers. This estimation is made by assuming the energy deposited across a calorimeter hit, that is one active and one absorber layer, is uniform. Working under this assumption, the total calorimeter hit energy is proportional to the active layer hit energy. This estimation procedure is loosely referred to as digitisation and, in this way, the cluster energy estimator introduced above can be written as

$$E_{Cluster} = \sum_{ECal\ hits,\ i} \epsilon^i_{ECal}\alpha_{ECal} + \sum_{HCal\ hits,\ i} \epsilon^i_{HCal}\alpha_{HCal} \ , \qquad (1.2)$$

where α_{ECal} and α_{HCal} are digitisation constants for the ECal and HCal respectively, ϵ^i_{ECal} is the ECal active layer hit energy for hit i and ϵ^i_{HCal} is the HCal active layer hit energy for hit i. The first stage of the calibration procedure presented in this chapter covers the determination of these digitisation constants, which convert the raw analogue-to-digital converter (ADC) response to a hit energy.

Once the basic energy estimator has been calibrated, it is possible to apply more advanced procedures designed to give a compensating calorimeter response [4]. A compensating calorimeter produces an identical response to a particle shower irrespective of whether the particle shower is electromagnetic or hadronic in nature. The primary cause of the difference in the response of a calorimeter to electromagnetic and hadronic showers is the undetectable energy component that is found in hadronic showers. These undetectable energy components are energy deposits produced from a showering particle that do

not produce a signal in the calorimeters. Hadronic showers contain this undetectable component due to a combination of effects such as neutrons stopping within the calorimeter and nuclear binding energy losses. Typically, this leads to calorimeters having a weaker response to hadronic showers than to electromagnetic showers.

There are two distinct routes available for achieving a compensating response from a calorimeter: the first is hardware compensation [5], whereby calorimeters are constructed using materials that yield extra energy in response to hadronic showers; and the second is software compensation [6], whereby the uncompensated calorimetric energies for hadronic showers are modified at the software level.

A novel example of hardware compensation is the ZEUS calorimeter [5]. The ZEUS calorimeter was constructed using uranium as the absorber material. In response to neutral hadrons the uranium undergoes fission producing extra energy that increases the hadronic response of the calorimeter. The amount of uranium was carefully chosen to achieve a fully compensating calorimeter response, i.e. identical calorimeter response to electromagnetic and hadronic showers. While hardware compensation is possible for the linear collider calorimeters, restrictions on calorimeter construction and the use of a large amount of radioactive material are highly undesirable.

The linear collider lends itself to software compensation as the fine segmentation of the calorimeters and precise reconstruction of individual particles makes identification of hadronic showers, and modifying their energies, feasible. A basic form of software compensation included in the linear collider reconstruction is the modification of the electromagnetic cluster energy estimator to

$$E_{EM\ Cluster} = \sum_{ECal\ hits,\ i} E^i_{ECal}\beta^{EM}_{ECal} + \sum_{HCal\ hits,\ i} E^i_{HCal}\beta^{EM}_{HCal} \ , \qquad (1.3)$$

and the hadronic cluster energy to

$$E_{Had\ Cluster} = \sum_{ECal\ hits,\ i} E^i_{ECal}\beta^{Had}_{ECal} + \sum_{HCal\ hits,\ i} E^i_{HCal}\beta^{Had}_{HCal} \ , \qquad (1.4)$$

where the βs are scaling factors that are applied to the energy of clusters of calorimeter hits associated with electromagnetic and hadronic clusters in the ECal and HCal. This simple scaling of energies compensates the response of the calorimeters, which leads to better detector performance. Determination of these energy scale setting constants is the second stage of the calibration procedure that is presented in this chapter.

While this scaling of energies improves detector performance, it does not account for any changes to the β scaling factors as a function of the total energy deposited. An energy dependence in the scaling factors is expected as the mechanisms governing the propagation of hadronic showers are sensitive to the shower energy [7]. To account for this, more sophisticated software techniques have been developed that vary the calorimeter cluster energy estimator as a function of energy to achieve a compensating response across a wider range of energies. These techniques make use of the fine segmentation of the linear collider calorimeters to identify hadronic showers. These techniques also address the problem of spuriously high energy calorimeter hits, which are caused by Landau fluctuations [8]. Landau fluctuations originate from high energy knock-on electrons appearing within particle showers [9] and can lead to overestimates of the particle shower energy if they occur in the active layers of a sampling calorimeter.

1.2 Calibration in the Particle Flow Paradigm

Calibration of the linear collider detector simulation is performed in to two processors in the software framework; the digitiser, which performs the digitisation process for sampling calorimeters, and PandoraPFA. The input to the digitiser is the active layer calorimeter response (ADC values) and the output is the combined, active and absorber layer, calorimeter hit energies. The hit energies are then used by PandoraPFA for event reconstruction. Calibration of the digitiser involves determining the digitisation constants (α_{ECal} and α_{HCal}) and the minimum ionising particle (MIP) scale, which is the average energy response for a MIP on a per hit basis. Similarly, calibration of PandoraPFA requires setting the scaling factors, β, and the MIP response using the combined calorimeter hit energies.

The α and β constants are determined by tuning the mean of reconstructed energy distributions. A number of cuts are applied when populating these reconstructed energy distributions that ensure the relevant reconstructed energy is being tuned. The application of these cuts means that linear scaling of the α and β constants does not lead to a linear shift in the mean of the reconstructed energy distributions. Therefore, when calibrating the α and β constants an iterative approach is taken; the next iteration of the calibration constant is determined by repeating the reconstruction using the current iteration of the constant and adjusting the constant based on the mean of the reconstructed energy distribution.

Determining the MIP scale is included in the calibration procedure as it is used by PandoraPFA in the identification of muons and for applying energy thresholds designed to limit the impact of noise. This energy scale is also used by the digitiser when simulating electrical noise, saturation effects in scintillator readout technologies and for applying noise vetoing energy thresholds [10].

The, non-zero, peak in the distribution of hit energies and ADC values for normally incident 10 GeV μ^- events is used to define the MIP scale in PandoraPFA and the digitiser respectively [9]. In the linear collider detector simulation, several realistic effects are simulated by the digitiser including saturation effects, energy thresholds, timing cuts and electrical noise. Application of these effects at this point in the software chain means that the active layer hit energies are not subject to them, while the post digitisation combined calorimeter hit energies are. Consequently, the MIP scale in PandoraPFA cannot be obtained from the digitiser MIP scale, instead both have to be independently determined.

Although this overall procedure is referred to as calibration, strictly speaking this is not correct. Calibration sets the detector response to real data, while this procedure sets the simulated detector response to Monte-Carlo (MC) events. In a real detector, calibration would follow the setting of the simulated detector response to MC events so that simulations can be used to guide the calibration process.

1.2.1 Overview of the Calibration Procedure

The calibration procedure is split into four separate operations: determination of digitisation constants (αs) in the digitiser; determination of scaling factor constants (βs) in PandoraPFA; MIP scale setting in the digitiser; and MIP scale setting in PandoraPFA. Calibration of the digitiser, digitisation constants and MIP scale, uses calorimetric energy measurements prior to any reconstruction, while calibration of PandoraPFA, scale factors and MIP scale, uses fully reconstructed particle flow objects (PFOs). As reconstructed PFOs are created using calorimetric energy measurements that have been digitised, it is wise to calibrate the digitiser before PandoraPFA, therefore, the calibration procedure is applied in the following order:

1. Setting the MIP response in the digitiser.

2. Setting the digitisation constants, αs, in the digitiser.

3. Setting the MIP response in PandoraPFA.

4. Setting the scaling factors, βs, in PandoraPFA.

1.2.2 MIP Scale Determination in the Digitiser

The MIP scale in the digitiser was determined by simulating 10 GeV μ^- events and creating a distribution of active layer calorimeter hit energies for each calorimeter in the detector simulation. When populating these distribution, a direction correction factor of $\cos(\theta)$, where θ is the incident angle of the μ^- to the calorimeter cell, was applied to account for the path length of the MIP through the active medium of the calorimeter. This converts the individual response to a normal-incident equivalent response. No selection cuts were applied to the sample of muon events.

Figure 1.1 shows the distribution used to determine the MIP peak in the ECal, HCal barrel, HCal endcap and HCal ring. In the digitiser software only a single HCal MIP scale, taken as the HCal barrel, is implemented.

1.2.3 Digitisation Implementation

This section discusses how the digitisation constants, αs, are determined. The digitisation constant for a given calorimeter depends upon several factors such as the material properties of the active and absorber layers, the magnetic field strength and energy losses occurring within the gaps in the detector. Therefore, each calorimeter in the ILD detector model has a distinct constant that must be determined independently.

1.2.3.1 ECal Digitisation Implementation

The procedure for determining the digitisation constants in the ECal involves simulation of single photons at an energy $E_{MC} = 10$ GeV. Single photons at this energy are largely contained within the ECal, as shown in figure 1.2a. This makes them ideal for isolating the ECal digitisation calibration from that of the HCal digitisation calibration. Events are only used for calibrating the ECal digitisation if they are confined to the ECal. To that extent, cuts are applied ensuring that the sum of the reconstructed energy found outside the ECal is less than 1% of E_{MC} and that the $\cos(\theta) < 0.95$, where θ is the polar angle of the photon. Photons that convert are also vetoed in this event sample at MC

(a)

(b)

(c)

(d)
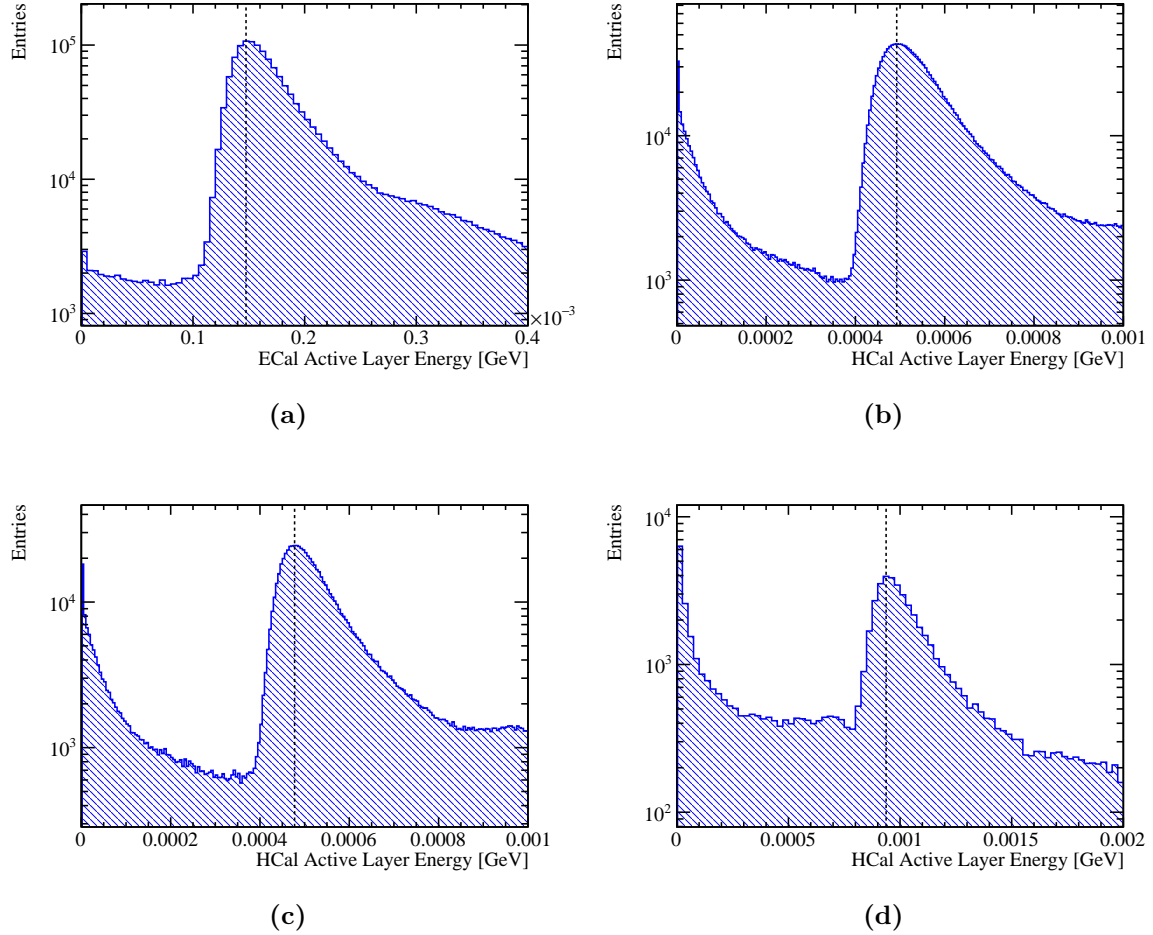
Figure 1.1: The active layer calorimeter hit energy distributions for (a) the ECal, (b) the HCal barrel, (c) the HCal endcap and (d) the HCal ring for 10 GeV μ^- events. The hit energies were corrected to account for the path length of the muons through the active medium of the calorimeter. The vertical black dotted lines indicate the position of the peak in each of these distributions that is used for defining the MIP scale in the digitisation processor.

level. The impact of these cuts on the sum of ECal hit energies for the $E_{MC} = 10$ GeV photons is shown in figure 1.2b.

The calibration of the digitisation in the ECal is an iterative procedure, which begins with the simulation of single photons using a trial calibration, α_{ECal}^0. Next the distribution of the sum of calorimeter hit energies within the ECal is produced for events passing the selection cuts, as shown in figure 1.2b. For an ideal calorimeter this distribution should be Gaussian, as described in chapter **??**, therefore, a Gaussian fit is applied to this distribution and the mean, E_{Fit}, extracted. To remove the effect of any outliers

(a)   **(b)**
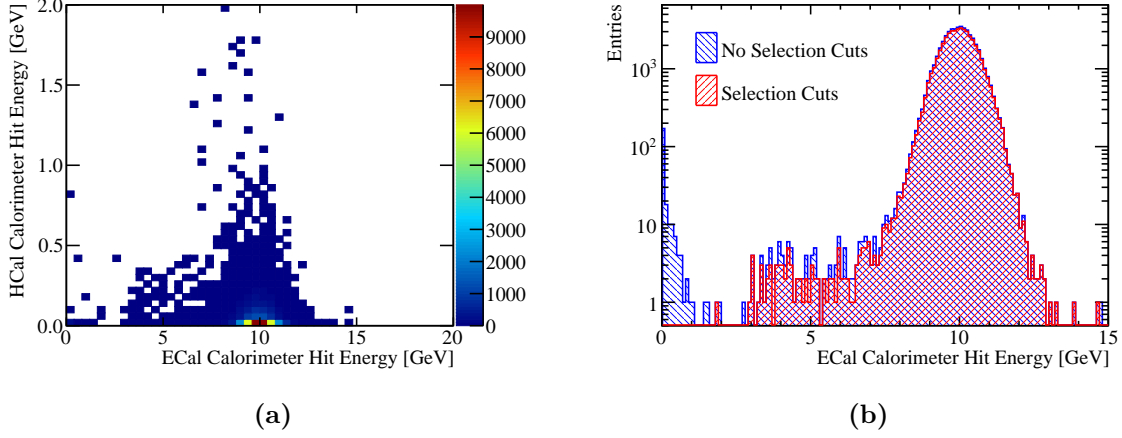
Figure 1.2: (a) The sum of calorimeter hit energies in ECal and HCal for 10 GeV photons. (b) The sum of the ECal calorimeter hit energies for 10 GeV photons with and without the selection cuts.

in this distribution, the fit is applied to the range of data with the smallest root mean square that contains at least 90 % of the data. An example of such a fit is shown in figure 1.3. In the case of ideal calibration, the mean of this fit, E_{Fit}, would be equal E_{MC}. It is assumed that any difference between the two is due to the calibration, therefore, to correct this the digitisation constant from the trial calibration, α^0_{ECal}, is rescaled by the ratio of the E_{MC} to E_{Fit}

$$\alpha^0_{\mathrm{ECal}} \to \alpha_{\mathrm{ECal}} = \alpha^0_{\mathrm{ECal}} \times \frac{E_{MC}}{E_{Fit}} \ . \tag{1.5}$$

This procedure is then repeated until the E_{Fit} falls within a specified tolerance of E_{MC}. The tolerance applied here was $|E_{\mathrm{Fit}} - E_{\mathrm{MC}}| < E_{\mathrm{MC}} \times 5\%$. The binning used for the fitted histogram is chosen such that the bin width is equal to the desired tolerance on E_{Fit} e.g. $E_{\mathrm{MC}} \times 5\% = 0.5$ GeV. It should be emphasised that the PFO energies used for downstream analyses have the electromagnetic and hadronic energy scale corrections applied, which are calibrated to a much tighter accuracy.

1.2.3.2 HCal Digitisation Implementation

The calibration for the digitisation in the HCal proceeds in a similar manner to that described for the ECal with a few key differences. This calibration uses simulated MC long-lived neutral kaons (K^0_Ls) at $E_{MC} = 20$ GeV. The higher energy, with respect to
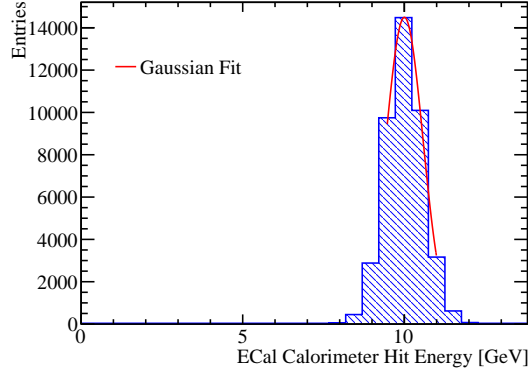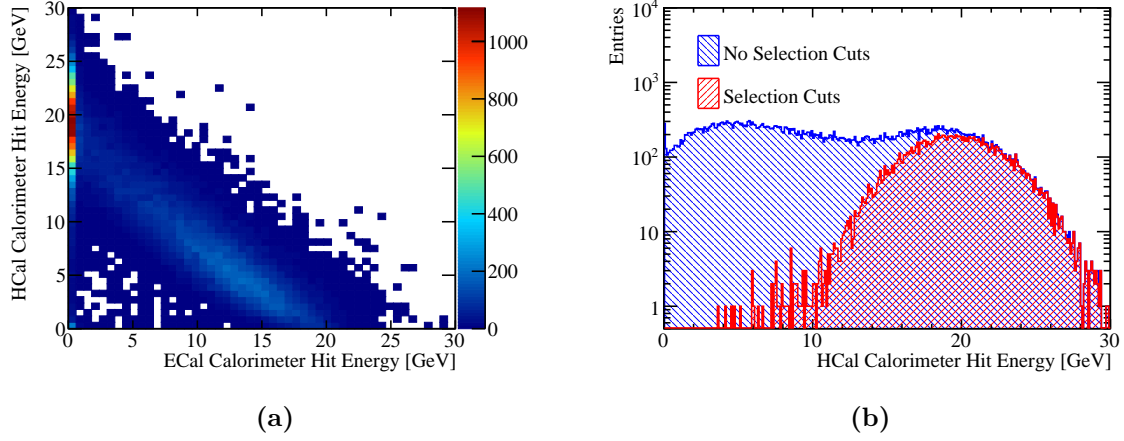
Figure 1.3: Gaussian fit to sum of the ECal calorimeter hit energies for 10 GeV photons with selection cuts. The coarse binning reflects the tolerance on the digitisation constant calibration.

the ECal digitisation, results in particle showers that sample deeper into the HCal. The K_L^0s must pass through the ECal, which contains one λ_I, before arriving at the HCal. Consequently, approximately 15% of these events begin showering in the ECal, as can be seen in figure 1.4a. Only events that deposit less than 5% of their energy in the ECal are used for calibrating the HCal digitisation constants. Furthermore, events that are not contained in the HCal are removed by requiring the last layer of the HCal where energy is deposited is required to be in the innermost 90% of the HCal. The impact of these cuts on the sum of HCal calorimeter hit energies for the $E_{MC} = 20$ GeV K_L^0 events is shown in figure 1.4b.

There are two HCal digitisation constants used in the detector simulation, one applied for the barrel and another for the endcap. The use of two digitisation constants accounts for differences in hadronic shower dynamics between the two, such as differing magnetic field configurations in the barrel and endcap. Both parameters are calibrated in the same manner, but have different cuts on θ, the polar angle of the K_L^0. For the barrel region of the HCal events are selected if $0.2 < \cos(\theta) < 0.6$, while for the endcap events are selected if $0.8 < \cos(\theta) < 0.9$. These angular cuts account for the transverse profile of the hadronic showers and ensure that the showers are largely confined to the relevant sub-detector. As many of the neutral hadrons appearing in jets are neutrons and their accessible energy is the kinetic energy as opposed to the total energy, the target reconstructed energy for these K_L^0 samples is the kinetic energy.

After applying the above K_L^0 selection cuts, the calibration procedure for the digitisation of the HCal barrel and endcap proceeds in the same manner as was described

(a)

(b)

Figure 1.4: (a) Sum of calorimeter hit energies in ECal and HCal for 20 GeV K_L^0 events. (b) Sum of the HCal calorimeter hit energies for a 20 GeV K_L^0 events with and without the selection cuts.

for the ECal. An example of the Gaussian fits applied to the sum of the calorimeter hit energies in the HCal barrel and endcap are shown in figure 1.5.

(a) HCal barrel.

(b) HCal endcap.
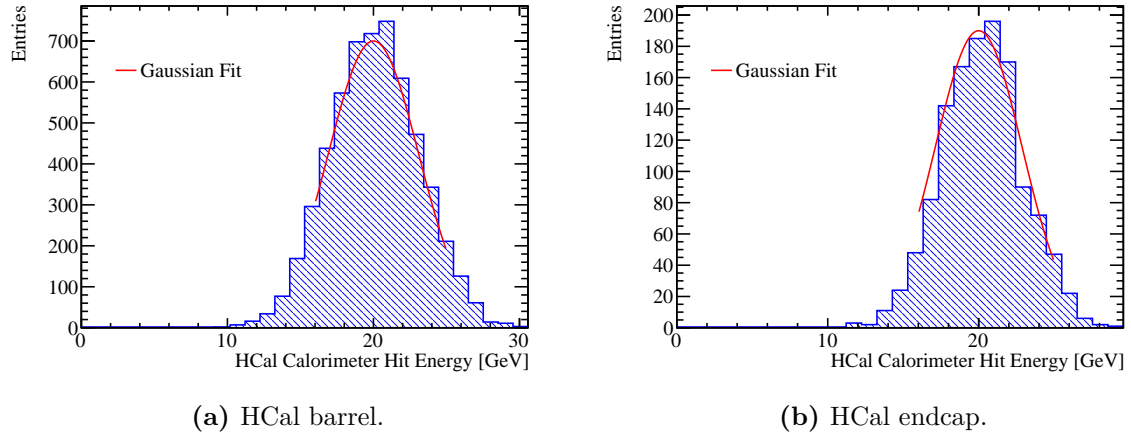
Figure 1.5: Gaussian fit to sum of the HCal calorimeter hit energies for 20 GeV K_L^0 events with selection cuts.

### 1.2.3.3 HCal Ring Digitisation Implementation

The HCal ring, as illustrated in figure 1.6, is a hadronic calorimeter that surrounds the ECal endcap and is sandwiched between the HCal barrel and endcap. This calorimeter

is required to ensure hermetic coverage of the hadronic calorimeter system across the barrel/endcap cross-over region [1].

The HCal ring has an independent digitisation constant to account for any difference in the hadronic shower development between the ring, barrel and endcap. Due to the thickness of the HCal ring, particle showers are never fully contained in it, so a different approach to calibration is required. To ensure that the HCal ring calibration is approximately correct, $\alpha_{\text{HCal ring}}$ is assumed to equal $\alpha_{\text{HCal endcap}}$ multiplied by several factors designed to account for differences in the active layer thickness, absorber layer thickness and the MIP response between the HCal endcap and ring. In detail

$$\alpha_{\text{HCal ring}} = \alpha_{\text{HCal endcap}} \times \frac{\langle \cos(\theta_{\text{endcap}}) \rangle}{\langle \cos(\theta_{\text{ring}}) \rangle} \times \frac{P_{\text{endcap}}}{P_{\text{ring}}} \times \frac{L_{\text{endcap}}^{Absorber}}{L_{\text{ring}}^{Absorber}} \times \frac{L_{\text{ring}}^{Active}}{L_{\text{endcap}}^{Active}} \ , \qquad (1.6)$$

where θ is the incident angle of the incoming particle to the calorimeter determined using the 20 GeV K_L^0s, L^{Active} is the active layer thickness and $L^{Absorber}$ is the absorber layer thickness. P is the position of the MIP peak in the distribution of active layer hit energies, which has been corrected so that the MIP appears to enter the calorimeter at normal incidence, and is determined using 10 GeV μ^- events.
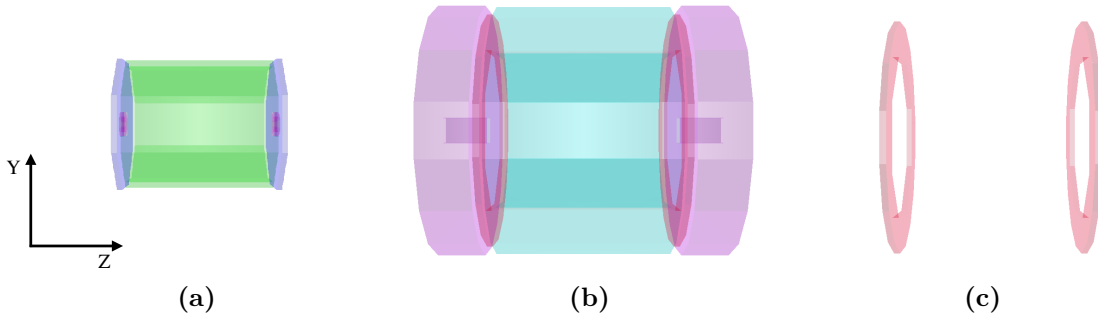
Figure 1.6: A PandoraPFA event display showing the nominal ILD calorimeters. (a) the ECal, (b) the full HCal and (c) the HCal ring, which covers the barrel/endcap cross-over region.

1.2.4 MIP Scale Determination in PandoraPFA

The MIP scale in PandoraPFA is set by simulating 10 GeV μ^- events and creating the distribution of combined calorimeter hit energies. The MIP scale in PandoraPFA must to be determined for the calorimeters and, in contrast to the digitiser, the muon chamber. Consequently, an additional distribution showing the calorimeter hit energy for

the muon chamber must be constructed at this stage of the calibration. As was done for the digitiser, a direction correction factor was applied to the hit energies account for the path length of the MIP through the active medium of the calorimeter and no selection cuts were applied.

Examples of the distributions used to set the MIP scale in PandoraPFA can be found in figure 1.7. Due to the energy thresholds applied in the digitiser, there are fewer populated bins with low hit energies. The double peak structure observed in the ECal calorimeter hit energy distribution is expected given the ECal absorber material thickness doubling in the back 10 layers of the ECal. The MIP peaks used for defining the MIP scale in PandoraPFA, figure 1.7, are broader than those used for determining MIP scale setting in the digitiser, 1.1, as the realistic effects applied by the digitiser are only present in the combined calorimeter hit energy distributions.

1.2.5 Electromagnetic Scale in PandoraPFA

Setting the electromagnetic scale in PandoraPFA is performed by examining the energies of particles reconstructed by PandoraPFA. The reconstruction is performed using the combined calorimeter hit energies that were set by the digitiser and having applied the noise vetoing MIP cuts.

The electromagnetic scale in the ECal, β_{ECal}^{EM}, is determined using simulated photons at $E_{MC} = 10$ GeV. To ensure that the events used for this part of the calibration are largely confined to the ECal, a cut requiring less than 1% of the reconstructed energy to be found outside the ECal is applied. Furthermore, only events reconstructed as a single photon are used to veto conversions. The impact of the selection cuts on the electromagnetic energy measured in the ECal for 10 GeV photons is shown in figure 1.8a. The peak at zero electromagnetic energy in the ECal is due to events traveling down the beam pipe and photon conversions. In photon conversion events, the calorimetric energy deposits made by the $e^{\pm}$ are associated to charged particle tracks. In this case, the energy measured using the calorimeters will be reported as zero because the charged particle tracks are used to determining the reconstructed particle energies. The tail of events with low electromagnetic energy in the ECal occurs primarily due pattern recognition failures in photon conversion events. In these events a small fraction of the calorimetric energy deposits made by the $e^{\pm}$ are not associated to charged particle tracks and instead are reconstructed as separate photons with a reconstructed energy much less than E_{MC}.

(a)

(b)

(c)
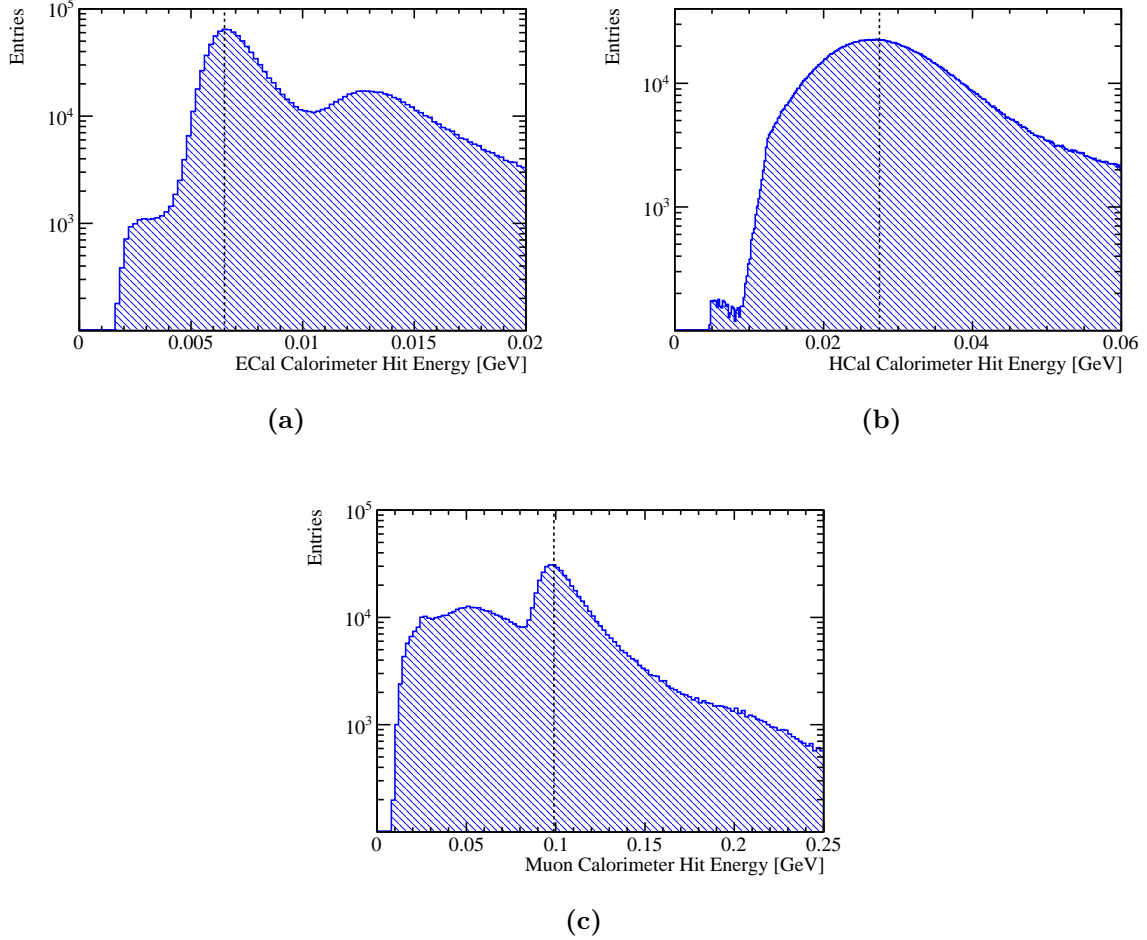
Figure 1.7: The combined calorimeter hit energy distributions for (a) the ECal, (b) the HCal and (c) the muon chamber for 10 GeV μ^- events. These hit energies were corrected to account for the path length of the muons through the active medium of the calorimeter. The vertical black dotted lines indicate the position of the peak in each of these distributions that is used for defining the MIP scale in PandoraPFA.

The fitting procedure follows that used for the ECal digitisation, described in section 1.2.3.1, whereby a trial calibration for the electromagnetic energy scale in the ECal, β_{ECal}^{EM0}, is first assumed. The initial trial calibration is approximate and is iteratively updated until it converges to within a chosen tolerance. Using the trial calibration, the photon events are reconstructed and the distribution of the electromagnetic energy in the ECal created. A Gaussian fit is then applied to this distribution in the range with the smallest root mean square containing at least 90 % of the data. The mean of the

fitted Gaussian, E_{Fit}, is then used to scale β_{ECal}^{EM0} in the following way

$$\beta_{ECal}^{EM0} \rightarrow \beta_{ECal}^{EM} = \beta_{ECal}^{EM0} \times \frac{E_{MC}}{E_{Fit}} \ . \tag{1.7}$$

An example distribution and fit used in the calibration of the nominal ILD detector model can be found in figure 1.8b. This procedure is repeated using the updated β_{ECal}^{EM} until E_{Fit} falls within a specified tolerance. The tolerance applied here was $|E_{\text{Fit}} - E_{\text{MC}}| < E_{\text{MC}} \times 0.5\%$. The binning for the fitted histogram is chosen such that the bin width is equal to the desired target tolerance on E_{Fit}, e.g. $E_{\text{MC}} \times 0.5\% = 0.05$ GeV. This tolerance is tighter than was applied for the digitisation as it is these and only these energies that are used in downstream analyses.

(a)

(b)
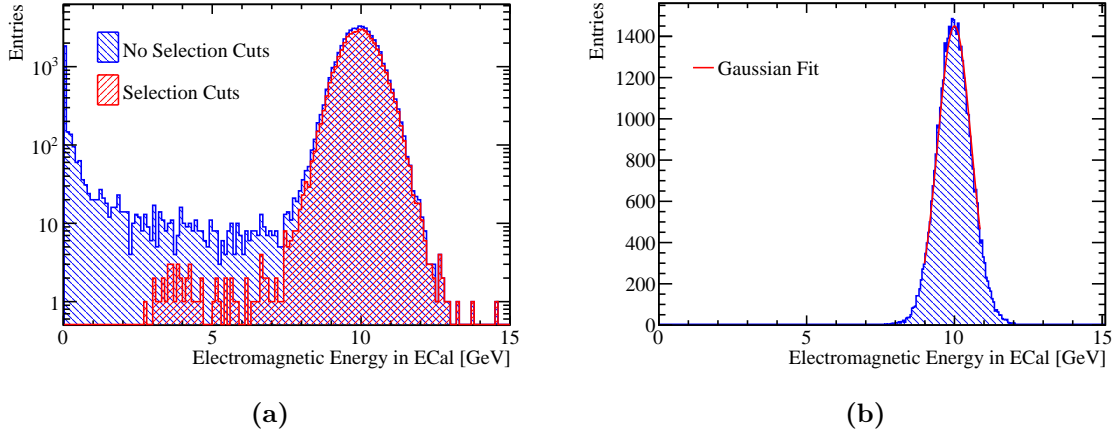
Figure 1.8: (a) The sum of the electromagnetic energy measured in the ECal for simulated 10 GeV photons with and without the selection cuts. (b) Gaussian fit to sum of the electromagnetic energy deposited in the ECal for simulated 10 GeV photons with selection cuts.

1.2.6 Hadronic Scale in PandoraPFA

The hadronic energy scale factors for the ECal, β_{ECal}^{Had}, and HCal, β_{HCal}^{Had}, are determined using simulated K_L^0 events at $E_{MC} = 20$ GeV. As the ECal contains approximately one nuclear interaction length, a non-negligible amount of hadronic energy will be deposited in the ECal, which makes the hadronic scale in the ECal, β_{ECal}^{Had}, important for detector performance. The hadronic scale in the ECal and HCal are simultaneously set as it is unfeasible to create a large sample of 20 GeV K_L^0s that are fully contained within the ECal.

For the reasons outlined in section 1.2.3.2, the target reconstructed energy for the sample of K_L^0s used for setting the hadronic energy scale is the kinetic energy, E_K, as opposed to the total energy. To ensure the events used are not affected by leakage of energy out of the back of the HCal, a cut is applied that vetoes events where energy is deposited in the outermost 10% of the HCal. In addition, a cut requiring a single neutral hadron to be reconstructed is applied to veto events with reconstruction failures and decays in the tracker. Finally, it is required that the total hadronic energy measured within the calorimeters falls within three σ of the kinetic energy of the K_L^0, where σ is taken to be $55\% \times \sqrt{E_K}$ GeV. This definition for σ is approximately the energy resolution for neutral hadrons using the nominal ILD HCal [1]. This cut ensures that when fitting the two dimensional distribution of hadronic energy measured in the ECal and HCal, outliers do not skew the fit. The impact of these selection cuts can be seen in figure 1.9.

(a)   (b)
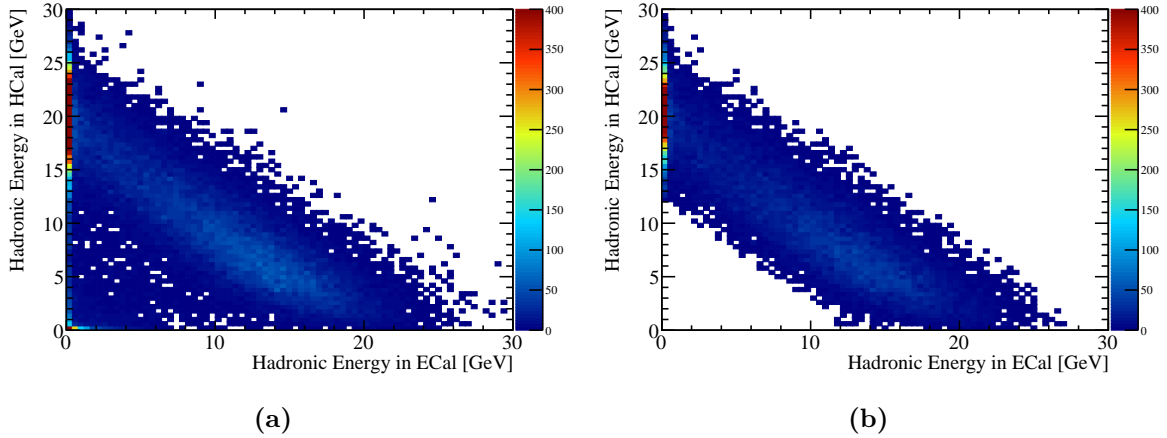
Figure 1.9: The distribution of hadronic energy measured in the ECal and HCal for 20 GeV K_L^0 events (a) without selection cuts and (b) with selection cuts.

Determining the hadronic scale in PandoraPFA is an iterative process and begins by assuming trial values, β_{ECal}^{Had0} and β_{HCal}^{Had0}, for the hadronic scale calibration factors β_{ECal}^{Had} and β_{HCal}^{Had}. The K_L^0 events are first reconstructed using the trial scale factors. Then a linear fit is applied to the two dimensional distribution of the reconstructed hadronic energies measured in the ECal and HCal for events passing the selection cuts. The best fit is obtained by minimising χ^2 with respect to variables describing a linear fit to the distribution. In this case, χ^2 is defined as

$$\chi^2(\delta_{ECal}^{Had}, \delta_{HCal}^{Had}) = \sum_i \left(\frac{r_i}{\sigma_{r_i}} \right)^2 , \qquad (1.8)$$

where r_i is the perpendicular distance in the two dimensional plane of hadronic energies measured in the ECal and HCal from the point (x_i, y_i) to a straight line passing through the points $(\delta_{ECal}^{Had}, 0)$ and $(0, \delta_{HCal}^{Had})$. In this definition, x_i and y_i are the hadronic energies measured in the ECal and HCal respectively for event i. The variables δ_{ECal}^{Had} and δ_{HCal}^{Had} describe a linear fit to the hadronic energy distribution, which are to be varied when minimising χ^2. The explicit definition of r_i is given in equation 1.9 and illustrated in figure 1.10. The uncertainty on r_i is given by σ_{r_i}, which is explicitly defined in equation 1.10. This uncertainty is calculated by propagating the uncertainties on x_i and y_i, which are assumed to be $\sigma_{x_i/y_i} = 55\% \times \sqrt{x_i/y_i}$, into the expression for r_i. The sum runs over all events, i, passing the selection cuts.

$$r_i = \frac{y_i \delta_{ECal}^{Had} + x_i \delta_{HCal}^{Had} - \delta_{ECal}^{Had} \delta_{HCal}^{Had}}{\sqrt{(\delta_{ECal}^{Had})^2 + (\delta_{HCal}^{Had})^2}} \ , \tag{1.9}$$

$$\sigma_i = \frac{(\sigma_{y_i} \delta_{ECal}^{Had})^2 + (\sigma_{x_i} \delta_{HCal}^{Had})^2}{\sqrt{(\delta_{ECal}^{Had})^2 + (\delta_{HCal}^{Had})^2}} \ . \tag{1.10}$$

The minimisation of χ^2 is done by stepping over a range of δ_{ECal}^{Had} and δ_{HCal}^{Had} centred about
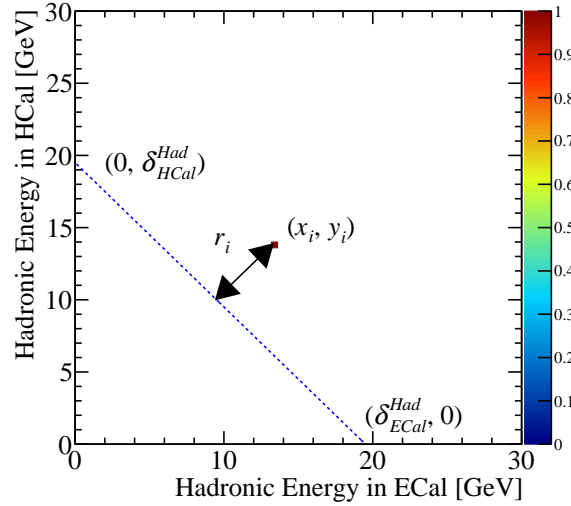
Figure 1.10: An example showing the definition of r_i. The blue dotted line corresponds to $y_i = \delta_{HCal}^{Had} - x_i \delta_{HCal}^{Had}/\delta_{ECal}^{Had}$.

the ideal value of E_K in search for the minimum χ^2. Once the minima in χ^2 is found the trial calibration factors β_{ECal}^{Had0} and β_{ECal}^{Had0} are rescaled to correct for any deviation from

the desired fit as follows

$$\beta_{ECal}^{Had0} \to \beta_{ECal}^{Had} = \beta_{ECal}^{Had0} \times \frac{E_K}{\Delta_{ECal}^{Had}} \ , \tag{1.11}$$

$$\beta_{HCal}^{Had0} \to \beta_{HCal}^{Had} = \beta_{HCal}^{Had0} \times \frac{E_K}{\Delta_{HCal}^{Had}} \ , \tag{1.12}$$

where Δ_{ECal}^{Had} and Δ_{ECal}^{Had} are the values of δ_{ECal}^{Had} and δ_{ECal}^{Had} giving the minimum χ^2. The step size used for minimising χ^2 with respect to δ_{ECal}^{Had} and δ_{ECal}^{Had} was chosen such that a single step would correspond to the final tolerance on δ^{Had}, which in this case is $\approx$ 0.1 GeV. This procedure is then repeated using the updated hadronic scaling factors until Δ_{ECal}^{Had} and Δ_{ECal}^{Had} both fall within a specified final tolerance, which in this case is taken to be $|\Delta_{E/HCal}^{Had} - E_K| < E_K \times 0.5\% \approx 0.1$ GeV.

The electromagnetic scale in the HCal, β_{HCal}^{EM}, is chosen to be equal to the hadronic scale in the HCal, β_{HCal}^{Had}. For the ILC and CLIC, β_{HCal}^{EM} is not a critical parameter in the reconstruction as photons are largely contained within the ECal meaning little to no electromagnetic energy is measured in the HCal.

Setting the hadronic scale in PandoraPFA ensures that the energy estimators for neutral hadrons are accurate at 20 GeV, however, this is not true for all energies. The undetectable energy component of a hadronic shower varies as a function of particle shower energy [7], which means the response of a calorimeter to neutral hadrons non-linear with the hadron energy. This is an inherent limitation of this calibration procedure that will be addressed by the development of more sophisticated energy estimators in subsequent chapters.

1.2.7 Summary

The procedure for setting the MC response in the linear collider detector simulation has been outlined. This procedure ensures that when modifying the detector simulation, the response of the detector will yield reliable energy estimators for particles showering in the calorimeter. For completion, after this calibration procedure has been applied, retraining of the likelihood data used by specific algorithms in PandoraPFA for the reconstruction of photons can be performed.

1.3 Novel Energy Estimators

This section describes two novel energy estimators that are introduced with a view to improving the energy resolution for hadronic showers. Two techniques will be discussed: HCal hit energy truncation, which focuses on limiting the impact of Landau fluctuations; and software compensation, which focuses on obtaining a compensating calorimeter response. Both of these techniques are implemented by introducing weights, ω^i, to calorimetric energy deposits made by showering particles in the HCal. The energy of a showering particle, $E_{Cluster}$, is determined by grouping together a clusters of calorimeter hits and summing their energies. When weights are applied to HCal hits this energy estimator becomes

$$E_{Cluster} = \sum_{ECal\ hits,\ i} E^i_{ECal} + \sum_{HCal\ hits,\ i} E^i_{HCal}\omega^i(\rho^i) \ . \qquad (1.13)$$

Weights are only applied to calorimeter hits in the HCal as these techniques modify the energy of hadronic showers, which are primarily contained within the HCal. The weights, ω^i, vary a function of the energy density of the calorimeter hit, $\rho^i = E^i_{HCal}/V$ where V is the physical volume of a calorimeter hit in the HCal, which includes the both the active and absorber layer thicknesses.

Although the exact weights depend on the implementation of the technique, a general feature is that at large E^i_{HCal} the weight is less than one. This limits the impact of spuriously high energy hits caused by Landau fluctuations. The energy loss probability distribution function for scintillator detectors, such as the ILD HCal, is given by a Landau function [8]. Energy deposits from the high energy tail of this distribution, which are known as Landau fluctuations, account for high energy knock-on electrons that appear within particle showers [9]. As Landau fluctuations deposit a disproportionately large amount of energy with respect to the bulk of the particle shower, they can lead to overestimates of the particle shower energy.

The energy loss probability distribution function for n particles passing through a calorimeter hit is given by the convolution of n Landau functions, which by the central limits theorem will tend to a Gaussian as n becomes large. Consequently, as the average number of particles passing through a calorimeter hit increases, the high energy tail in the energy loss probability distribution function for the hit becomes less pronounced and the impact of Landau fluctuations decreases. This means that the impact of Landau fluctuations on energy measurements is dictated by the density of a particles within a

particle shower and the transverse segmentation, or cell size, of the calorimeter in use. If the transverse segmentation, or cell size, of a calorimeter decreases, the average number of particles passing through each hit decreases and the impact of Landau fluctuations increases. Any technique used for minimising the impact of Landau fluctuations will be sensitive to the transverse segmentation of the calorimeters in use.

1.3.1 HCal Hit Energy Truncation

The first technique to be examined is a simple truncation of the hadronic energy, E, recorded in any given HCal hit

$$E \to E' = \begin{cases} E & \text{if } E < \kappa , \\ \kappa & \text{otherwise} , \end{cases} \tag{1.14}$$

where κ is the value of the truncation. This improves the energy estimators for hadronic clusters by limiting the impact of Landau fluctuations. In terms of ω introduced in equation 1.13 the truncation corresponds to

$$\omega(\rho) = \begin{cases} 1 & \text{if } \rho \times V < \kappa , \\ \frac{\kappa}{\rho \times V} & \text{otherwise} . \end{cases} \tag{1.15}$$

This weight as a function of hit energy density is shown in figure 1.11.
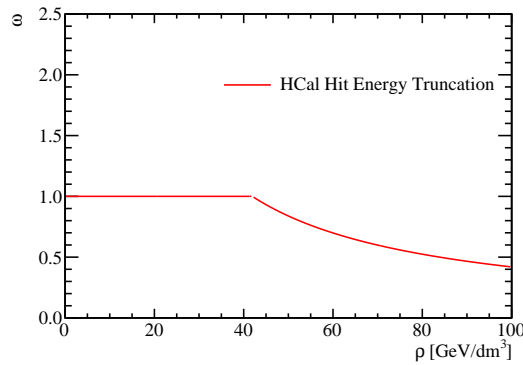
Figure 1.11: The weights, ω, used in the HCal hit energy truncation as a function of the energy density of the HCal hit, ρ. The truncation shown here corresponds to a 1 GeV truncation in the nominal ILD HCal.

1.3.1.1 Legacy Energy Corrections

Alongside the HCal hit energy truncation, PandoraPFA also applied two other energy corrections designed at limiting the impact of Landau fluctuations. They are:

- **Clean Clusters**. This algorithm checks to see whether the energy measured within a calorimeter hit is anomalously high. Anomalously high energy hits are defined as hits where the energy contained within the hit is greater than 10% of the energy of the cluster that the hit has been associated to. If a hit is deemed to have an anomalously high energy and if this energy is above a threshold (0.5 GeV) the hit energy used by PandoraPFA is modified. The updated hit energy is taken as the average hit energy in the calorimeter layers immediately before and after the layer containing the high energy hit.

- **Scale Hot Hadrons**. This algorithm calculates the average energy of the calorimeter hits in a given cluster cluster in units of, normally incident, MIP equivalent particles. If this number is larger than a certain value, default 15 MIPs per hit, the cluster energy is rescaled to give a lower average number of MIPs per hit, default is 5 MIPs per hit.

In the reconstruction, these corrections are applied to each cluster of calorimeter hits, irrespective of the location of that cluster in the detector. These algorithms, with the HCal hit truncation, form the "legacy" energy corrections that are used by PandoraPFA when performing the event reconstruction.

1.3.1.2 Impact on Single Particle Energy Resolution

Figure 1.12a shows the energy resolution for neutral hadrons as a function of the HCal hit energy truncation. The optimal truncation for the ILD detector model simulation was 1 GeV and, using this truncation, a neutral hadron energy resolution of $\sim 8.8\% = 62\%/\sqrt{E(\mathrm{GeV})}$ was obtained for $E = 50~GeV$ K_L^0 events. In comparison, the neutral hadron energy resolution for $E = 50~GeV$ K_L^0 events obtained without a truncation was $\sim 10.4\% = 74\%/\sqrt{E(\mathrm{GeV})}$. Smaller energy truncations begin to truncate the energy of calorimeter hits produced in typical hadronic shower development, while larger truncations allow for a larger impact from Landau fluctuations. Both of these effects result in worsening neutral hadron energy resolutions. For completeness the photon energy resolutions as a function of HCal hit energy truncation are shown in figure 1.12b.

As expected the photon energy resolution is unaffected by the HCal hit energy truncation as the photons are largely contained within the ECal.
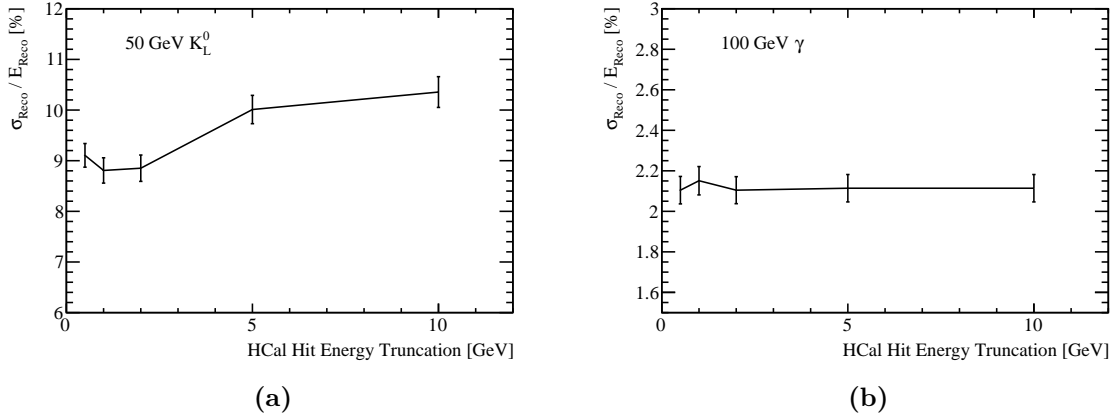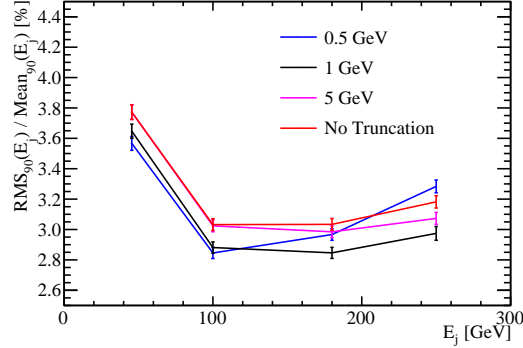

Figure 1.12: The energy resolution as a function of HCal cell truncation for (a) 50 GeV K_L^0 events and (b) 100 GeV photon events using the nominal ILD detector model.

1.3.1.3 Impact on Jet Energy Resolution

Figure 1.13 shows the jet energy resolution as a function of jet energy for selected values of the HCal hit energy truncation. The trends in this plot are complex as the optimal HCal hit energy truncation varies with the jet energy. For 45.5 GeV jets, the best jet energy resolution, $\sim 3.6\%$, is obtained using a 0.5 GeV truncation, while for 180 GeV jets, the best jet energy resolution, $\sim 2.9\%$, is obtained using a 1 GeV truncation. This is expected because at low jet energies the average number of particles passing through each active calorimeter hit will be small, meaning the impact of Landau fluctuations is large and that to limit them a low truncation energy is needed. As the jet energy increases more particles on average pass through each calorimeter hit and the impact of Landau fluctuations decreases.

It is clear that a 1 GeV HCal hit energy truncation is beneficial for the performance of the nominal ILD detector model since the jet energy resolution is reduced by roughly $\sim 0.15\%$ across the jet energy range from 45.5 GeV to 250 GeV. As the HCal hit truncation technique offers significant performance gains, it is used for the calorimeter optimisation studies presented in chapter **??**. These studies include optimisation of the HCal cell size. Increasing the HCal cell size will increase the average number of particles passing through each calorimeter hit, which in turn reduces the impact of Landau fluctuations and vice

Figure 1.13: The jet energy resolution as a function of jet energy for various HCal hit energy truncations. The results shown use the nominal ILD detector model, which contains 30×30 mm^2 square scintillator tiles in the HCal.

verse. For all detector models considered where the HCal cell size was varied, the HCal hit energy truncation was reoptimsied to account for the changing impact of Landau fluctuations. For detector models with a HCal cell size of 10×10 mm^2, 20×20 mm^2, 30×30 mm^2, 40×40 mm^2, 50×50 mm^2 and 100×100 mm^2 the reoptimised truncation values were 0.5, 0.75, 1, 1.5, 2 and 5 GeV respectively. Furthermore, the average particle density in a HCal hit will also be sensitive to the properties of the absorber material used in the calorimeters, therefore, the HCal hit energy truncation was also reoptimised in the HCal absorber material study. The optimal truncation energy cut for the 30×30 mm^2 cell size tungsten HCal option was 5 GeV, while for all other detector models considered it was 1 GeV. The cause of increased truncation energy cut for tungsten is discussed in section **??**.

Understanding the affect of the HCal hit energy truncation is crucial when performing optimisation studies. This can be seen in figure 1.14, which shows the results of the HCal cell size optimisation study when using a 1 GeV truncation and when optimising the truncation for each detector model. By applying a uniform HCal hit energy truncation the importance of the HCal cell size to particle flow calorimetry is vastly overinflated. For example, if the HCal cell size is increased from 10 mm to 100 mm the jet energy resolution for 250 GeV jets goes from $\sim 2.8\%$ to $\sim 4.5\%$ for the flat 1 GeV truncation, but only $\sim 3.5\%$ when using an optimised truncation. As the jet energy and HCal cell size increase, the flat 1 GeV truncation throws away a larger fraction of typical hadronic shower energy measurements, which causes the jet energy resolution to degrade rapidly.
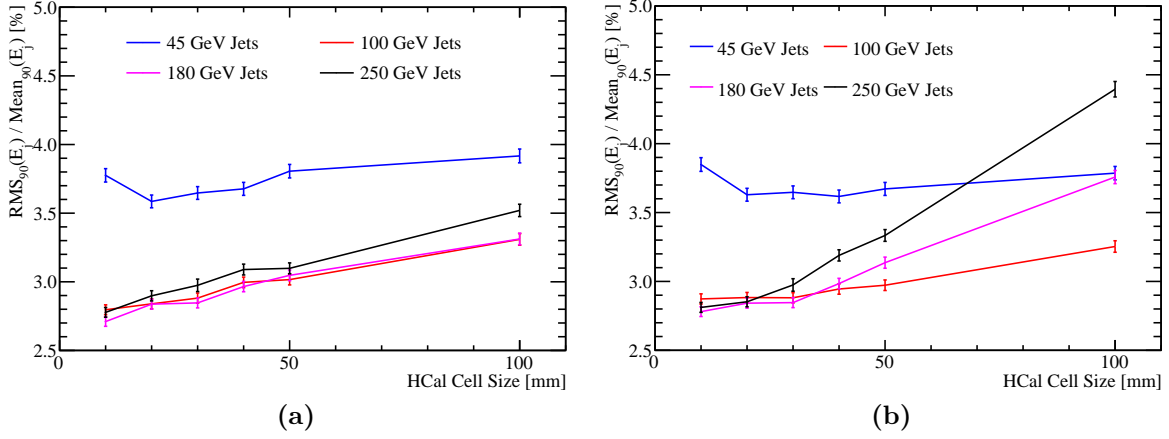
Figure 1.14: The jet energy resolution as a function of HCal cell size in the ILD detector model using a HCal hit energy truncation that is (a) optimised and (b) fixed at 1 GeV.

1.3.2 Software Compensation

Particle showers that are produced when a hadron interacts with a calorimeter contain two components [7]; an electromagnetic shower core, which originates from the production and decay of π^0s and ηs, and a hadronic shower component originating from other interacting and decaying particles. By identifying each of these components in the reconstruction, it is possible to modify their energies to give a compensating calorimeter response. This technique known as software compensation.

Software compensation achieves a compensating calorimeter response by applying weights, as introduced in equation 1.13, that modify the energy of calorimeter hits in the HCal. These weights increase the energy found in the hadronic hits to compensate for the undetectable energy component found in hadronic showers. Additionally, these weights reduce the energy of spuriously high energy hits to minimise the impact of Landau fluctuations. The weights vary as a function of the calorimeter hit energy density, ρ^i, and the uncompensated energy of the particle shower, E_{Raw}, where

$$E_{Raw} = \sum_{ECal\ hits,\ i} E^i_{ECal} + \sum_{HCal\ hits,\ i} E^i_{HCal} \ . \tag{1.16}$$

The electromagnetic and hadronic components of a hadronic particle shower are treated differently in this approach by applying wights that are sensitive to the energy density of the calorimeter hits. Hits with large energy densities are likely to be part of the electromagnetic core, while low energy density hits are likely to be part of satellite

hadronic hits around the electromagnetic shower core [11]. By tailoring the weights as a function of the energy density, a compensating calorimeter response can be obtained. Figure 1.15 shows the electromagnetic and hadronic shower components, determined by the energy density of the calorimeter hits, for a hadronic shower in a 500 GeV Z→uds di-jet event.

(a)   (b)
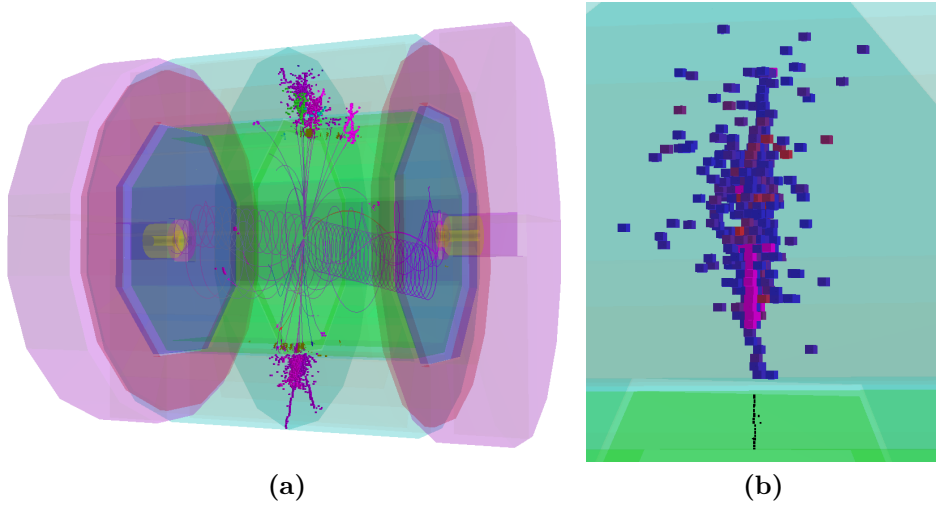
Figure 1.15: An event display for a 500 GeV Z→uds di-jet event reconstructed using the nominal ILD detector. (a) The full event environment. (b) A single hadronic cluster from the same event where shading indicates the energy density in the HCal. High energy density cells are coloured red, while lower energy density cells are coloured blue. All ECal hits are shaded black. The high energy density electromagnetic core of the selected hadronic cluster is clearly visible.

The software compensation weights also depend on E_{Raw}, the total raw cluster energy, to account for the sensitivity of the hit energy density distribution on the total particle shower energy. For hadronic showers, the fraction of the total energy carried in the electromagnetic core increases as the total shower energy increases [7], therefore a dependancy of the weights on E_{Raw} is needed to obtain a compensating calorimeter response across a wide range of energies.

The precise form of the weights used in this technique are [11]

$$\omega(E_{Raw}, \rho) = p_1(E_{Raw}) \times \exp(p_2(E_{Raw}) \times \rho) + p_3(E_{Raw}) \ , \tag{1.17}$$

$$\tag{1.18}$$

with

$$p_1(E_{Raw}) = p_{11} + p_{12} \times E_{Raw} + p_{13} \times E_{Raw}^2 \qquad (1.19)$$

$$p_2(E_{Raw}) = p_{21} + p_{22} \times E_{Raw} + p_{23} \times E_{Raw}^2 \qquad (1.20)$$

$$p_3(E_{Raw}) = \frac{p_{31}}{p_{32} + \exp(p_{33} \times E_{Raw})} \ , \qquad (1.21)$$

where $p_{\alpha\beta}$ are constants and

$$E_{Raw} = \sum_{ECal \ hits, \ i} E_{ECal}^i + \sum_{HCal \ hits, \ i} E_{HCal}^i \ . \qquad (1.22)$$

The parameters $p_{\alpha\beta}$ were determined by minimising $\chi^2(p_{\alpha\beta})$ where

$$\chi^2(p_{\alpha\beta}) = \sum_{Events} \left(\frac{(E_{Cluster}^{SC}(p_{\alpha\beta}) - E_{MC})}{0.5 \times \sqrt{E_{MC}}} \right)^2 \qquad (1.23)$$

where the sum runs over single K_L^0 events that ranged in energy from 10 to 100 GeV in steps of 10 GeV. At each energy the same number of events was used to avoid biasing to particular energies. In each event, $E_{Cluster}^{SC}$ is the software compensated energy estimator for the reconstructed event and E_{MC} is the MC energy of the K_L^0. Normalising the deviation of $E_{Cluster}^{SC}$ from E_{MC} by the stochastic term in the HCal energy resolution, $\sim 50\% \times \sqrt{E}$, made sure events of different MC energy contributed the same weight to χ^2.

Figure 1.17 shows $\omega(E_{Raw}, \rho)$ as a function of ρ for selected values of E_{Raw} and figure 1.16 shows $p_1(E_{Raw})$, $p_2(E_{Raw})$ and $p_3(E_{Raw})$ as a function of E_{Raw}. These weights shown in figures 1.17 and 1.16 were obtained by training the software compensation technique on samples simulated using the nominal ILD detector model. Figure 1.17 shows that the high energy density hits are being reduced in energy to compensate for the effects of Landau fluctuations, while the low energy density hits are being increased in weight to compensate for the undetectable energy component found in hadronic showers. Furthermore, the weights vary as a function of the raw hadronic shower energy to account for the changing energy density topology of hadronic showers with increasing shower energy.

This technique is applied in the PandoraPFA framework in the form of an energy correction function, which means whenever the energy of a cluster of hits is considered by PandoraPFA the software compensated energy is used. Applying software compensation
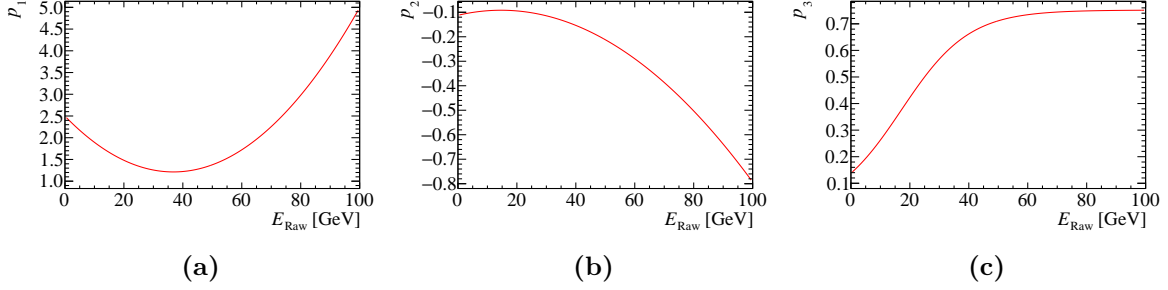
Figure 1.16: Parameters used in software compensation weight determination as a function of E_{Raw}.
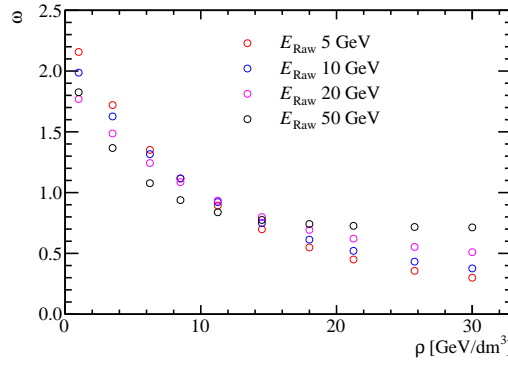
Figure 1.17: The software compensation weight applied to a calorimeter hit as a function of calorimeter hit energy density for various cluster energies.

in this way benefits the detector energy resolution in two ways; firstly, the intrinsic energy resolution of the detector improves and secondly, the confusion contribution to the energy resolution is reduced.

As software compensation only modifies the energy of HCal hits there is freedom to apply further energy corrections to the ECal hits. Applying the "Clean Clusters" logic, described in section 1.3.1.1, to the ECal hits alongside software compensation was found to be beneficial to the jet energy resolution. Therefore, the application of software compensation within PandoraPFA implicitly involves the application of the "Clean Clusters" logic to the ECal hits.

Software compensation was tuned using a maximum K_L^0 energy of 100 GeV, therefore, it is only applied to clusters where $E_{Raw} < 100$ GeV as sensible behaviour outside this range cannot be ensured. While it would be possible to modify the energy range of

the training sample to go to higher energies, hadronic clusters with energy greater than 100 GeV will be rare at the ILC like energies considered here.

1.3.2.1 Impact on Single Particle Energy Resolution

Figure 1.18 shows the energy resolution as a function of MC energy for single K_L^0 events obtained using various energy correction configurations in PandoraPFA. When comparing the energy resolution given by software compensation to that obtained using no energy corrections, it can be seen that software compensation offers an improvement in the energy resolution of $\sim 15\%$ across the energy range considered. The uniformity of this improvement is encouraging, indicating that software compensation is achieving a compensating calorimeter response across this wide range of energies.

Comparing the performance of software compensation to the legacy corrections, described in section 1.3.1.1, it can be seen that software compensation gives a better energy resolution across almost the entire range of energies considered. The only exception to this is around $E_{K_L^0} \sim 50$ GeV where the performance of software compensation and the legacy corrections are comparable. By removing the hit truncation from the legacy options it is clear that the changes in energy resolution when using the legacy options are being driven by the hit truncation. This makes the trend in energy resolution observed using the legacy corrections clear as, at low K_L^0 energies, very few hits are affected by the truncation so the performance is comparable to not using any energy corrections. At high K_L^0 energies, the truncation is too aggressive and removes energy from hits that are not spuriously high leading to a worsening energy resolution. Between these two extremes, $E_{K_L^0} \sim 50$ GeV, the truncation works ideally and the improvement in energy resolution when using the legacy corrections is the largest.

1.3.2.2 Impact on Jet Energy Resolution

The improvements in the intrinsic energy resolution of the detector observed when using software compensation will propagate into the reconstruction of jets. Figure 1.19 shows the jet energy resolution as a function of jet energy when using selected energy correction configurations in PandoraPFA. It can be seen that software compensation is extremely beneficial to the detector performance as applying it improves the jet energy resolution by $\sim 15\%$ across the energy range considered in comparison to using no energy corrections. Furthermore, software compensation offers an improvement in the jet energy resolution
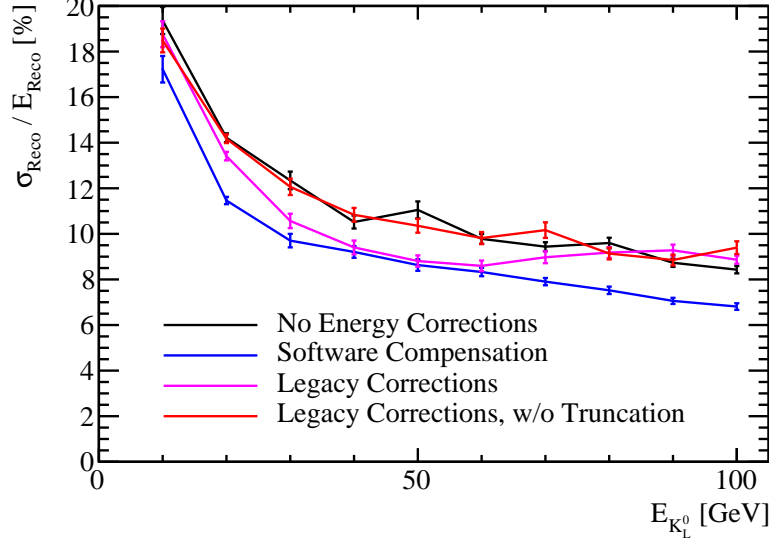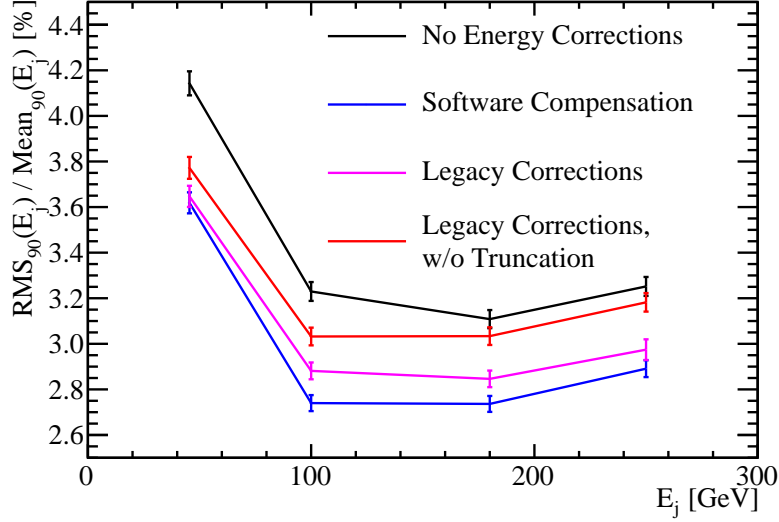
Figure 1.18: The energy resolution as a function of the MC energy for single K_L^0 events using various energy correction settings. The black line represents no energy corrections, the blue line represents software compensation, the magenta line represents the legacy energy corrections and the red line represents the legacy corrections without the HCal hit energy truncation. The nominal ILD detector model was used in these simulations.

of the order of 5% for jet energies $\gtrsim 100$ GeV in comparison to the legacy corrections, which prior to the development of software compensation had given the best jet energy resolutions.

Further light can be shed on these trends by examining the contributions to the jet energy resolution from the intrinsic energy resolution of the detector and the pattern recognition confusion, which are shown in figure 1.20. The intrinsic energy resolution contribution shows that software compensation is significantly better than all other energy corrections options, which is to be expected from the energy resolution studies presented in section 1.3.2.1. When compared to the legacy energy corrections, software compensation improves the intrinsic energy resolution by up to 12% across the energy range considered, with the largest improvement occurring for 100 GeV jets. As jets contain a broad spectrum of hadronic cluster energies, there is no jet energy for which the intrinsic energy resolution of the detector is comparable between the legacy corrections and software compensation. The confusion contributions to the jet energy resolution when using software compensation and the legacy corrections are almost identical. This indicates that the improvement seen in the jet energy resolution when comparing software
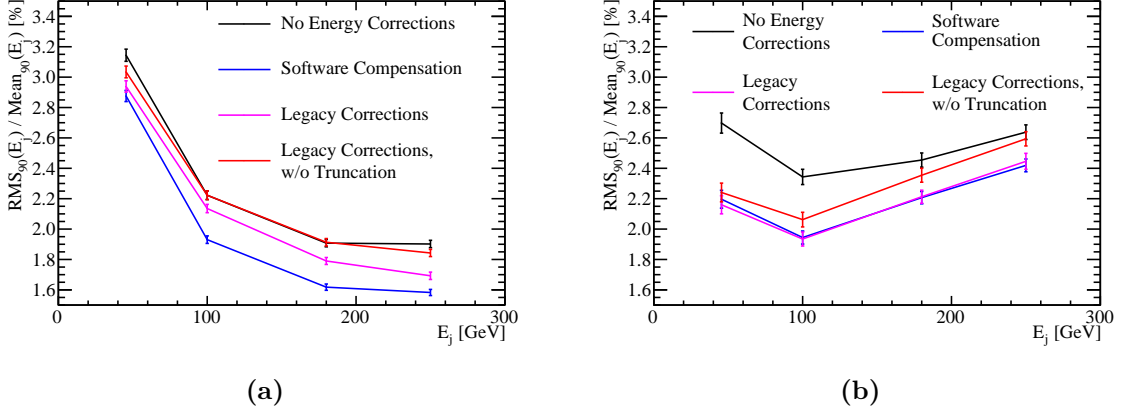
Figure 1.19: The jet energy resolution as a function of the jet energy for a variety of different energy correction options. The black line represents no energy corrections, the blue line represents software compensation, the magenta line represents the legacy energy corrections and the red line represents the legacy corrections without the HCal hit energy truncation. The nominal ILD detector model was used in these simulations.

compensation to the legacy corrections, shown in figure 1.19, is being driven by the intrinsic energy resolution.

The "Clean Clusters" and "Scale Hot Hadrons" energy corrections, i.e. the legacy corrections without the HCal hit energy truncation, benefits the pattern recognition by reducing the confusion contribution. The confusion contribution is reduced by $\sim 18\%$ for 45.5 GeV jets using these energy corrections, however, as the jet energy increases the magnitude of this improvement decreases, such that at 250 GeV jets no improvement is seen. These corrections do not significantly affect the intrinsic energy resolution of the detector. As these corrections benefit pattern recognition, selected aspects of their logic is applied to ECal hits in the software compensation energy correction as previously discussed.

1.3.3 Summary

The effect on both single particle and jet energy resolution of the HCal hit energy truncation and software compensation have been examined. Although relatively simplistic,

Figure 1.20: The contributions to the jet energy resolution as a function of the jet energy for a variety of different energy correction options. The jet energy resolution contributions presented are (a) the intrinsic energy resolution of the detector and (b) the total confusion contribution. The jet energy resolution obtained using the standard reconstruction is given by the quadrature sum of the intrinsic energy resolution and total confusion contributions. The black line represents no energy corrections, the blue line represents software compensation, the magenta line represents the legacy energy corrections and the red line represents the legacy corrections without the HCal hit energy truncation. The nominal ILD detector model was used in these simulations.

the HCal hit energy truncation was found to be beneficial for detector performance by limiting the impact of Landau fluctuations. The more sophisticated software compensation procedure was found to be highly effective at producing a compensating calorimeter response across a wide range of energies, which translated into excellent performance in terms of jet energy resolution.

1.4 Timing Cuts

The linear collider will operate using trigger-less readout whereby the recorded data for each sub-detector is read out between collisions of the e^+ and e^- bunches. The bunch train structure for ILC and CLIC is compared in table 1.1. Event selection will proceed through the application of a software trigger. This involves the identification of any hard interactions, prior to full event reconstruction, and only putting data into the event reconstruction if it is measured within a chosen time window about these interactions. The recorded time of a calorimeter hit, which is cut on to make the time window for the software trigger, is corrected for straight time-of-flight to the IP. This ensures that the

amount of time particle showers have to develop in the calorimeters is independent of their position in the detector. As the width of this time window changes, the amount of time particle showers have to develop changes, which will affect the performance of the detector.

At CLIC, the application of a software trigger is challenging due to the 0.5 ns bunch separation. At CLIC, the integration time of the calorimeters will span many bunch crossings and, due to the intense beam-induced backgrounds, identifying energy deposits produced from the hard interaction of interest is difficult. By placing tight timing constraints on the energy deposits made in the CLIC calorimeters, it is possible to minimise the impact of the beam-induced backgrounds. As well as minimising the impact of the backgrounds, these tight timing requirements will also truncate the shower development time for hard interaction of interest. Understanding the impact of these timing requirements on physics performance is vital to the success of the CLIC experiment. Timing cuts are not as challenging at the ILC because the bunch separation is much larger, meaning the calorimeters could be read out between bunches, and the beam-induced backgrounds are much smaller.

	ILC 500 GeV	CLIC 3 TeV
Electrons per bunch [10^{10}]	2.0	0.37
Bunches per train	2820	312
Train repetition rate [Hz]	5	50
Bunch separation [ns]	308	0.5

Table 1.1: The train structure for 500 GeV ILC and 3 TeV CLIC [1, 2].

For all choices of time window considered in this study the calibration procedure described in section 1.2 was reapplied. This ensures that the mean of the reconstructed energy distributions will be invariant to changes in the calorimeter timing window as the calibration procedure compensates for any energy losses incurred by truncating the particle shower development time.

For results presented in this chapter and the optimisation studies found in chapter **??** a 100 ns timing window was applied to all detector models considered. As the choice of timing window has yet to be finalised for the linear collider this value was chosen as it represents something that could be achieved using the readout technology options presently available [12].

1.4.1 Impact on Single Particle Energy Resolution

The energy resolution for 100 GeV photon and 50 GeV K_L^0 events as a function of the timing window applied to the calorimeter hits is shown, for the nominal ILD detector, in figure 1.21. The timing cut makes little difference to the energy resolution of the photon events, however, the energy resolution for neutral hadrons gets significantly worse as the time window is reduced. The neutral hadron energy resolution becomes worse by almost 20 % when the time window is reduced from 10^6 ns to 10 ns. These trends are to be e expected as electromagnetic showers develop far more rapidly than their hadronic counterparts [7]. This can be seen in figure 1.22, which shows the distribution of the measurement time of calorimeter hits, corrected for time-of-flight, for selected shower components within 91 GeV Z→uds di-jet events. Hadronic showers develop slowly as they often involve intermediate states that must decay to continue the propagation of the shower. If a narrow calorimeter timing window is used, energy measurements from the hadronic shower will be lost and the energy resolution will degrade, which is what is observed.
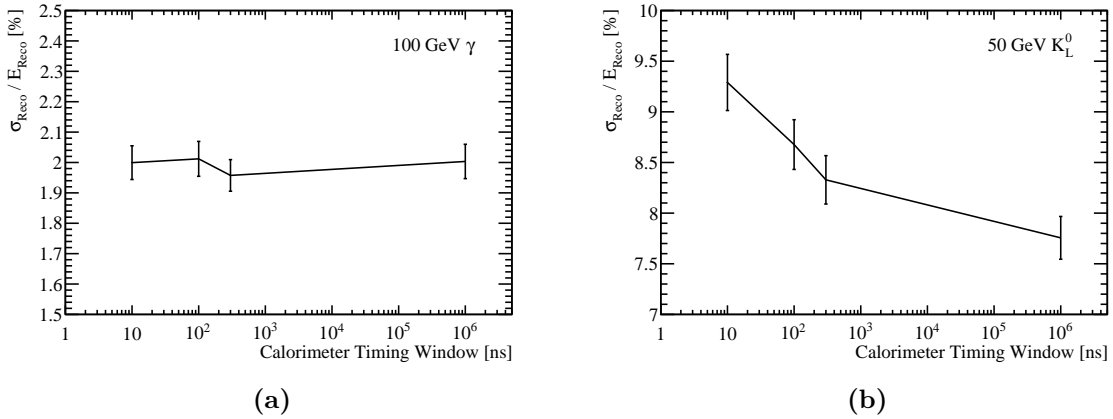
Figure 1.21: The energy resolution as a function of calorimeter timing window for (a) 100 GeV photon events and (b) 50 GeV K_L^0 events using the nominal ILD detector model.

1.4.2 Impact on Jet Energy Resolution

The jet energy resolution as a function of the jet energy for selected calorimeter time windows is shown in figure 1.23. As expected, the jet energy resolution will also be affected by the reduced neutral hadron energy resolution when the calorimeter timing window is reduced. The sole exception to this is the 250 GeV jets for the 100 ns time
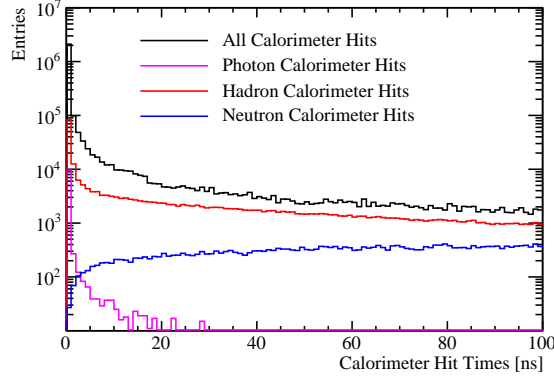
Figure 1.22: The distribution of the time of the calorimeter hits, corrected for time of flight to the impact point, for 91 GeV Z→uds di-jet events. Electromagnetic shower energy deposits, i.e. photon calorimeter hits, are deposited very rapidly, while hadronic shower energy deposits are deposited over a much longer time period.

window whereby the jet energy resolution is slightly better than when using the 300 ns and semi-infinite time windows, although this is not statistically significant.
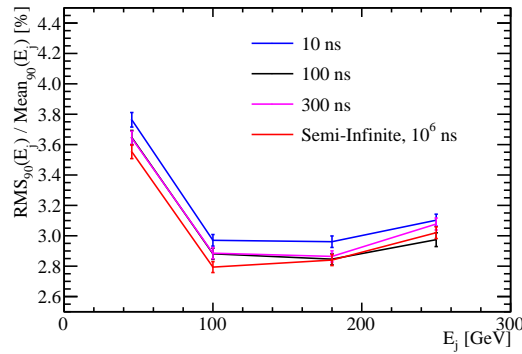
Figure 1.23: The jet energy resolution as a function of jet energy for various calorimeter timing cuts. The nominal ILD detector model was used in these simulations.

The time window applied to the calorimeter hits affects both the neutral hadron and jet energy resolutions with a larger timing window leading to better resolutions. It can be seen that applying an aggressive choice of time window, such as 10 ns, the jet energy resolution is degraded as many of the hadronic showers being sampled do not have time to fully develop. However, even using a 10 ns timing cut the jet energy resolutions are still sufficiently low to give excellent detector performance. Both the single particle and jet energy resolutions indicate that the majority of hadronic showers will have fully developed within 100 ns and that there are little gains to be made by extending the size of this window.

1.4.3 Summary

Simulations were performed where the size of the calorimeter hit time window used in the software trigger at the linear collider experiments was varied to determine what impact it had on physics performance. The energy resolution for electromagnetic showers did not change significantly when varying the size of time window, however, the neutral hadron energy resolution became worse as the size of the time window was reduced. The jet energy resolution was also sensitive to the size of the time window used, however, the trend was far weaker than that seen for neutral hadrons. There were no major benefits to increasing the time window beyond 100 ns indicating that this time is sufficient for the bulk of hadronic showers to develop.

Chapter 2

The Sensitivity of CLIC to Anomalous Gauge Couplings through Vector Boson Scattering

"Kids, you tried your best, and you failed miserably. The lesson is, never try."

— Homer Simpson

2.1 Motivation

Vector boson scattering is the interaction of the form VV → VV where V is any of the electroweak gauge bosons W$^+$, W$^-$, Z or γ. This is an interesting process to study because it provides understanding of how the Standard Model Higgs is able to unitarise the otherwise unbounded cross-section for longitudinal massive gauge boson scattering. Vector boson scattering also provides insights into beyond standard model physics that impacts the electroweak sector by probing potential anomalous triple and quartic gauge couplings.

Triple and quartic gauge couplings lead to interactions of the form V → VV and VV → VV respectively. In the Standard Model there are five allowed vertices, shown in figure 2.1, which arise from the kinematic term $\mathcal{L}_{kin} = -\frac{1}{4}B_{\mu\nu}B^{\mu\nu} - \frac{1}{4}W_{\mu\nu}W^{\mu\nu}$ in the Standard Model Lagrangian.
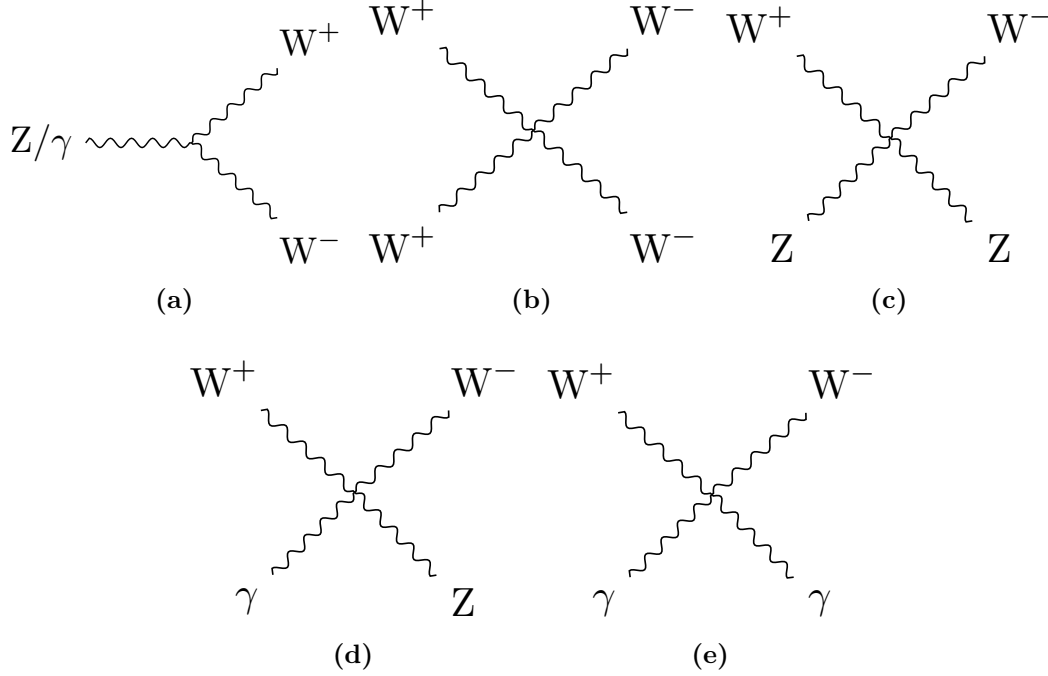
Figure 2.1: Triple and quartic gauge boson vertices in the Standard Model.

Anomalous triple and quartic gauge couplings are introduced as parameters in effective field theories (EFTs). These couplings either modify the Standard Model triple and quartic gauge boson vertices or introduce new triple and quartic vertices that were previously forbidden. EFTs are a mathematical construct designed to introduce new physics in a manner that builds upon the Standard Model. They work under the assumption that new physics exists at an energy scale, Λ, that is much higher than the energy scales currently accessible to modern day particle physics experiments. In the limit $\Lambda \to \infty$, the Standard Model is reproduced as the new physics becomes kinematically inaccessible. Such theories are model independent, giving them a wide span in the search for new physics. A classic example of an EFT theory is the Fermi theory for beta decay [13]. At energies much below the mass of the W boson, the weak interaction occurring when a neutron decays into a proton, electron and anti-neutrino can be treated as a four-point vertex with quartic coupling strength G_F, the Fermi Coupling constant as shown in figure 2.2.

The study presented in this chapter examines the anomalous quartic gauge couplings α_4 and α_5 through vector boson scattering process. The anomalous gauge couplings that are to be examined are introduced as part of an EFT that is described in chapter **??**.
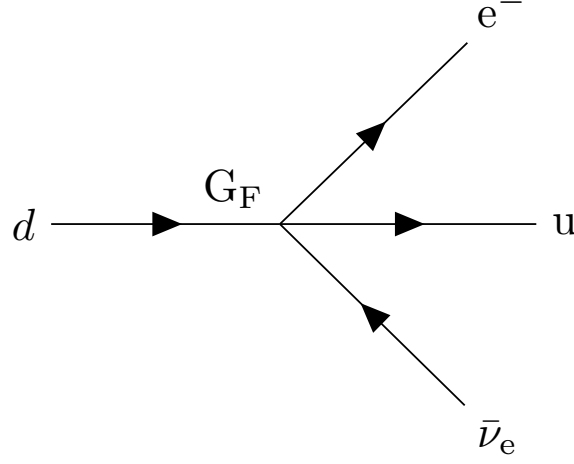
Figure 2.2: Four-point vertex proposed for explanation of beta decay by Fermi.

These couplings appear in the Lagrangian through the following terms

$$\alpha_4[\text{Tr}(V^\mu V_\mu)]^2 \quad \text{and} \quad \alpha_5 \text{Tr}(V^\mu V_\nu)]\text{Tr}(V^\nu V_\mu)] \;, \tag{2.1}$$

where V_μ corresponds, in a carefully chosen gauge, to a linear combination of the massive gauge bosons W^+, W^- and Z. These terms modify the Standard Model vertices $W^+W^- \to W^+W^-$ and $W^+W^- \to ZZ$ as well as introducing the new vertex $ZZ \to ZZ$. The anomalous gauge couplings α_4 and α_5 can be studied in vector boson scattering processes such as those shown in figure 2.3.

CLIC is designed for precision measurements in e^+e^- collisions at high energies and it is ideal for a study of vector boson scattering. The application of Particle Flow Calorimetry with fine granularity calorimeters gives CLIC excellent jet energy resolution, which allows it to clearly characterise multi-jet final states and final states containing missing energy in the form of neutrinos. The excellent jet energy resolution also allows for accurate separation of W and Z bosons through di-jet invariant mass, which will be invaluable for event selection.

The cross-sections for vector boson scattering processes are sufficiently large at the proposed running energies for CLIC to give large signal sample sizes. A study of anomalous gauge boson couplings at CLIC has the potential to give results several orders of magnitude better than the complementary studies performed at the LHC because of the reduction in hadronic backgrounds and increased cross-section for vector boson
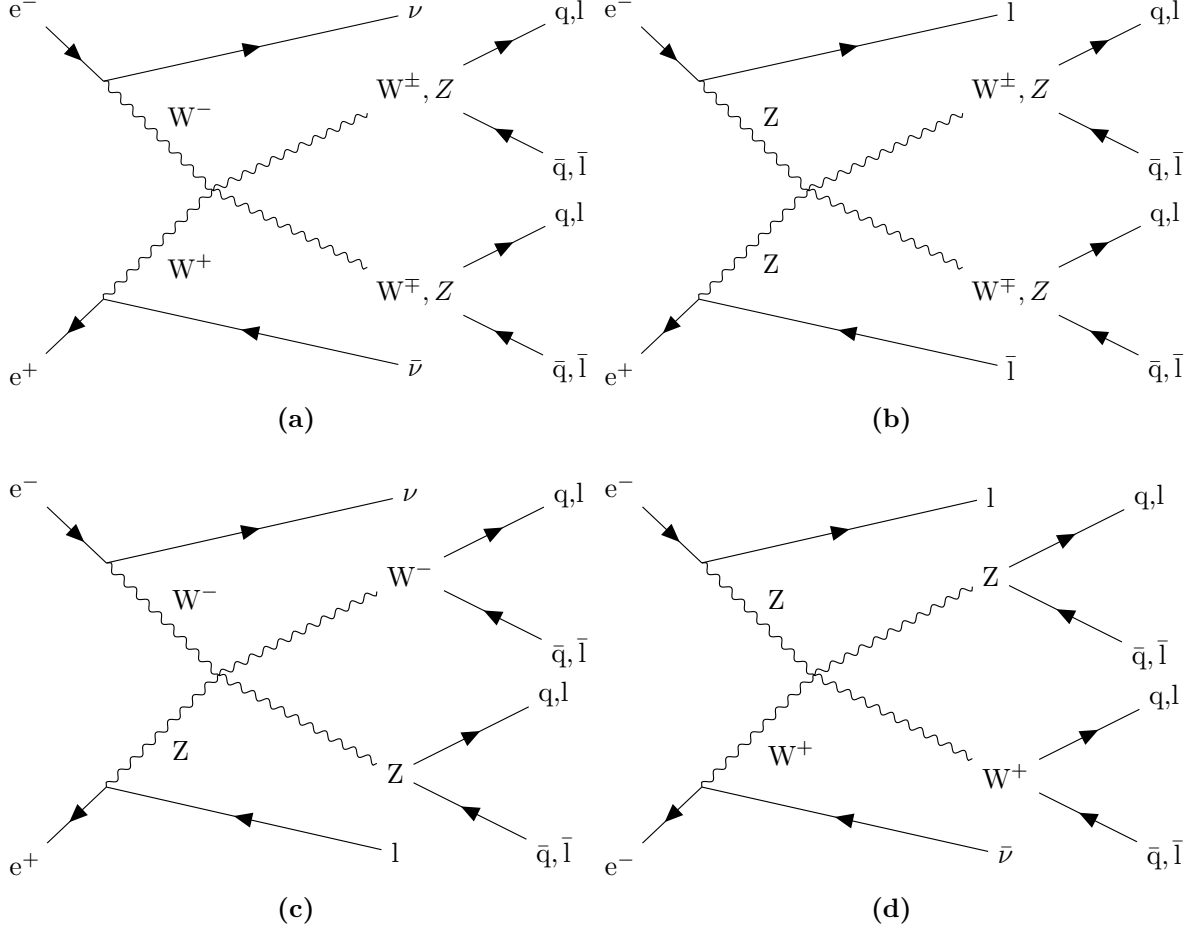
Figure 2.3: Example of vector boson scattering Feynman diagrams showing sensitivity to quartic gauge boson self-interaction vertices. The processes shown are relevant for CLIC. In these diagrams q represents the u, d, s, c and b quarks; l represents e^-, μ^- and τ^- leptons; and ν represents the ν_e, ν_μ and ν_τ neutrinos.

scattering processes [14]. The above reasons make a strong case for performing a vector boson scattering analysis at CLIC.

The branching fractions for the hadronic decays of both the $W^\pm$ and Z bosons is of the order of 70% [15], therefore, the signal final states for the analysis presented in this chapter are vector boson scattering processes where the outgoing bosons decay purely hadronically: $\nu\nu$qqqq, νlqqqq and llqqqq.

2.2 Event Generation, Simulation and Reconstruction

Events were generated using Whizard [16, 17] version 1.95. Due to the presence of beamstrahlung photons in the CLIC beam, events were generated for collisions of e^+e^-, $e^+\gamma$, γe^- and $\gamma\gamma$. The energy spectra used for all particles involved in these collisions took into account the effects of radiation in the form of beamstrahlung photons and the intrinsic energy spread of the CLIC beam. Furthermore, events involving the interaction between the electromagnetic field of the beam particles involving quasi-real photon mediators with low momenta, described by the Weizsacker-Williams approximation or the Equivalent Photon Approximation (EPA), were generated using Whizard and included in this analysis. Fragmentation and hadronisation was implemented using PYTHIA 6.4 [18] that was tuned for OPAL e^+e^- collision data recorded at LEP [19]. The decays of tau leptons was simulated using TAUOLA [20]. The full list of events used in this analysis, along with their Standard Model cross-section for $\sqrt{s} = 1.4$ TeV can be found in table 2.1. The samples comprise all final states that are relevant, either as signal or background processes, for an analysis involving the purely hadronic decay channels from the vector boson scattering process:

- Final states from the purely hadronic decay channels of the vector boson scattering process. These states are expected to show sensitivity to the anomalous couplings α_4 and α_5: $e^+e^- \to \nu\nu qqqq$, $e^+e^- \to \nu lqqqq$ and $e^+e^- \to llqqqq$

- Final states with four primary quarks arising from e^+e^- interactions: $e^+e^- \to qqqq$.

- Final states with two primary quarks arising from e^+e^- interactions: $e^+e^- \to \nu\nu qq$, $e^+e^- \to \nu lqq$, $e^+e^- \to llqq$ and $e^+e^- \to qq$.

- Final states with four primary quarks arising from the interactions of either e^+ or e^- with a beamstrahlung photon: $e^-\gamma_{BS} \to e^- qqqq$, $e^+\gamma_{BS} \to e^+ qqqq$, $e^-\gamma_{BS} \to \nu_e qqqq$ and $e^+\gamma_{BS} \to \bar{\nu}_e qqqq$.

- Final states with four primary quarks arising from the interactions of either e^+ or e^- with the electromagnetic field of the opposing beam particle. These cross-sections are calculated using the EPA approximation, which represents the electromagnetic field of the opposing beam particle as a series of photons, so the final states appear as interactions of e^+ or e^- with photons: $e^-\gamma_{EPA} \to e^- qqqq$, $e^+\gamma_{EPA} \to e^+ qqqq$, $e^-\gamma_{EPA} \to \nu_e qqqq$ and $e^+\gamma_{EPA} \to \bar{\nu}_e qqqq$.

- Final states with four primary quarks arising from the interaction of the electromagnetic fields of opposing beam particles using the EPA approximation: $\gamma_{\mathrm{EPA}}\gamma_{\mathrm{EPA}} \rightarrow$ qqqq.

- Final states with four primary quarks arising arising from the interaction of the electromagnetic field of either e^+ or e^- using the EPA approximation with a beamstrahlung photon: $\gamma_{\mathrm{EPA}}\gamma_{\mathrm{BS}} \rightarrow$ qqqq or $\gamma_{\mathrm{BS}}\gamma_{\mathrm{EPA}} \rightarrow$ qqqq.

- Final states with four primary quarks arising from the interaction of two beamstrahlung photons: $\gamma_{\mathrm{BS}}\gamma_{\mathrm{BS}} \rightarrow$ qqqq.

In the above list q represents u, $\bar{\mathrm{u}}$, d, $\bar{\mathrm{d}}$, s, $\bar{\mathrm{s}}$, c, $\bar{\mathrm{c}}$, b or $\bar{\mathrm{b}}$; l represents $e^\pm$, $\mu^\pm$ or $\tau^\pm$; and ν represents ν_{e}, $\overline{\nu}_{\mathrm{e}}$, ν_μ, $\overline{\nu}_\mu$, ν_τ and $\overline{\nu}_\tau$.

Monte-Carlo (MC) samples were simulated using the CLID_ILD detector model [21]. Further details of this detector model can be found in chapter **??**. The simulation was performed in MOKKA [22], which is a GEANT4 [23] wrapper providing detailed geometric descriptions of detector concepts for the linear collider. Events were reconstructed using the MARLIN [24] c++ framework, designed for reconstruction at the linear collider. PandoraPFA [4, 25] was used to apply Particle Flow Calorimetry in the reconstruction, the full details of which can be found in chapter **??**.

The effect of the $\gamma\gamma \rightarrow hadrons$ backgrounds, discussed in section **??**, were incorporated in the analysis by overlaying $\gamma\gamma \rightarrow hadrons$ events onto the signal and background event samples. The overlaid backgrounds were added prior to reconstruction so that their impact on the reconstruction was fully accounted for. For each physics event of interest, $\gamma\gamma \rightarrow hadrons$ background events equivalent to 60 bunch crossings (BXs) are included. As readout time windows are applied in detector readout, 60 BXs is sufficient for accounting for the $\gamma\gamma \rightarrow hadrons$ backgrounds. These backgrounds occur in a time window of -5 ns to 25 ns around the physics event and the BXs are separated by 0.5 ns, to mimic the CLIC bunch train structure. The number of background events overlaid per BX is drawn from a Poisson distribution with a mean of 1.3 (3.2) events per bunch crossing at $\sqrt{s} = 1.4$ (3) TeV [2].

Detector readout is simulated using a readout time window, of 10 ns on all detectors apart from the TPC and HCal barrel. All hits are kept in the TPC, while a 100 ns time window is used in the HCal barrel to account for the additional time it takes hadronic showers to develop in tungsten. All readout times are corrected for straight time-of-flight

Final State	Cross Section [fb]
$e^+e^- \rightarrow \nu\nu qqqq$	24.7
$e^+e^- \rightarrow \nu lqqqq$	110.4
$e^+e^- \rightarrow llqqqq$	62.1
$e^+e^- \rightarrow qqqq$	1245.1
$e^+e^- \rightarrow \nu\nu qq$	787.7
$e^+e^- \rightarrow \nu lqq$	4309.7
$e^+e^- \rightarrow llqq$	2725.8
$e^+e^- \rightarrow qq$	4009.5
$e^-\gamma_{\mathrm{EPA}} \rightarrow e^- qqqq$	287.1
$e^-\gamma_{\mathrm{BS}} \rightarrow e^- qqqq$	1160.7
$e^+\gamma_{\mathrm{EPA}} \rightarrow e^+ qqqq$	286.9
$e^+\gamma_{\mathrm{BS}} \rightarrow e^+ qqqq$	1156.3
$e^-\gamma_{\mathrm{EPA}} \rightarrow \nu_e qqqq$	32.6
$e^-\gamma_{\mathrm{BS}} \rightarrow \nu_e qqqq$	136.9
$e^+\gamma_{\mathrm{EPA}} \rightarrow \overline{\nu}_e qqqq$	32.6
$e^+\gamma_{\mathrm{BS}} \rightarrow \overline{\nu}_e qqqq$	136.4
$\gamma_{\mathrm{EPA}}\gamma_{\mathrm{EPA}} \rightarrow qqqq$	753.0
$\gamma_{\mathrm{EPA}}\gamma_{\mathrm{BS}} \rightarrow qqqq$	4034.8
$\gamma_{\mathrm{BS}}\gamma_{\mathrm{EPA}} \rightarrow qqqq$	4018.7
$\gamma_{\mathrm{BS}}\gamma_{\mathrm{BS}} \rightarrow qqqq$	21406.2

Table 2.1: Cross sections of signal and background processes for $\sqrt{s} = 1.4$ TeV. In the above table q represents u, $\bar{\mathrm{u}}$, d, $\bar{\mathrm{d}}$, s, $\bar{\mathrm{s}}$, c, $\bar{\mathrm{c}}$, b or $\bar{\mathrm{b}}$; l represents $e^\pm$, $\mu^\pm$ or $\tau^\pm$; and ν represents ν_e, $\overline{\nu}_e$, ν_μ, $\overline{\nu}_\mu$, ν_τ and $\overline{\nu}_\tau$. The EPA and BS subscript on the incoming photon indicates whether the photon is generated from the equivalent photon approximation or beamstrahlung.

to the impact point (IP). Any hits that have are measured outside of these windows are not used in the reconstruction.

2.3 Modelling of Anomalous Gauge Couplings

The samples that were sensitive to the anomalous gauge couplings α_4 and α_5 were generated using Whizard version 1.97, instead of the previously quoted version 1.95. This change was required as version 1.97 contained a unitarisation scheme that ensured

cross-sections for processes involving longitudinal gauge boson scattering did not violate unitarity at the energies considered here.

Two alternative methods exist for modelling the sensitivity of the vector boson scattering process to the anomalous gauge couplings α_4 and α_5. The first is to generate multiple samples with different values of α_4 and α_5 and the second is to generate a single sample with $\alpha_4 = 0$ and $\alpha_5 = 0$ and reweight that sample. The latter approach was taken in this analysis as the former approach is impractical when considering a fine sampling of the α_4 and α_5 space.

Event weights, w, are calculated according to the ratio of the matrix elements, M, for the particular event configuration [26]

$$w(\alpha_4, \alpha_5) = \frac{|M(event, \alpha_4, \alpha_5)|^2}{|M(event, 0, 0)|^2}. \tag{2.2}$$

Figure 2.4 shows the dependence of the event weights on α_4 and α_5 for four individual $\nu\nu$qqqq final state events, generated for $\sqrt{s} = 1.4$ TeV.

Only final states involving contributions from massive gauge boson quartic vertices require reweighting. Whizard was used to evaluate the cross-sections for all final states shown in table 2.1 with $\alpha_4 = \alpha_5 = 0$ and with $\alpha_4 = \alpha_5 = 0.05$. Only the three final states shown in table 2.2 were found to have a dependency on α_4 and α_5.

Final State	Cross Section [fb] ($\alpha_4 = \alpha_5 = 0.00$)	Cross Section [fb] ($\alpha_4 = \alpha_5 = 0.05$)	Percentage Change[%]
$e^+e^- \to \nu\nu$qqqq	24.7	34.6	+40.1
$e^+e^- \to \nu$lqqqq	115.3	113.0	-2.0
$e^+e^- \to$ llqqqq	62.1	68.6	+10.5

Table 2.2: Cross sections for selected processes showing the effect of the anomalous gauge couplings α_4 and α_5 for $\sqrt{s} = 1.4$ TeV.

To maximise the sensitivity to the anomalous gauge couplings, the $\nu\nu$qqqq final state is used to define signal in this analysis. The lνqqqq and llqqqq final states are treated as backgrounds that are invariant to changes in α_4 and α_5 because they have a much reduced sensitivity to the anomalous gauge couplings in comparison to the $\nu\nu$qqqq final state. Furthermore, the lνqqqq and llqqqq final states can be easily vetoed during event selection because of the presence of the primary lepton, which means the sensitivity of
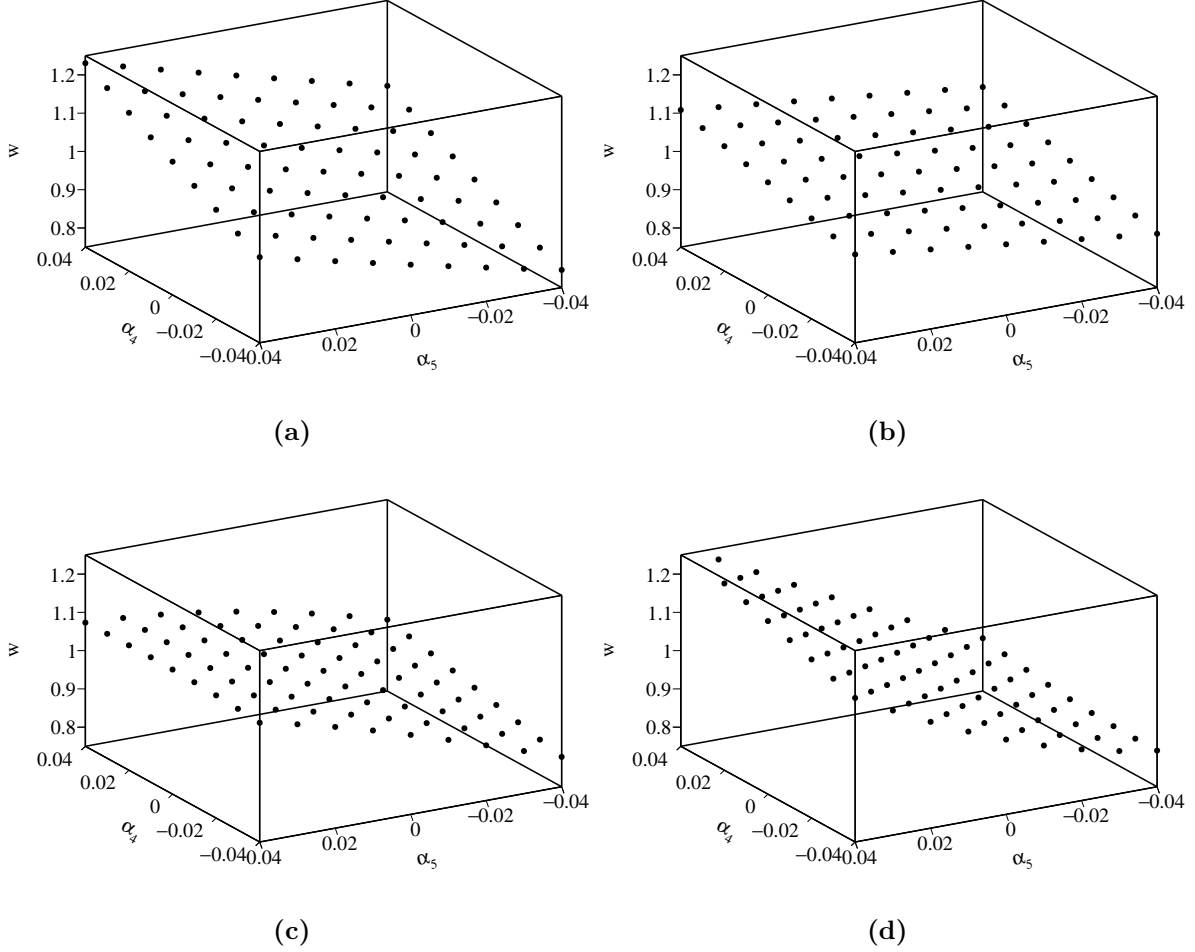
Figure 2.4: The event weights, w, determined by the generator as a function of the anomalous couplings α_4 and α_5 for a selection of $\nu\nu$qqqq final state events for $\sqrt{s} = 1.4$ TeV.

these states to the anomalous gauge couplings will have a negligible effect on the results from this study.

Use of the unitarisation scheme in Whizard 1.97, which is needed to ensure cross-sections do not violate unitarity when studying anomalous gauge couplings at CLIC like energies, requires a unit CKM matrix [26]. The impact of this requirement was examined by comparing several reconstructed and MC distributions for $\nu\nu$qqqq final state events generated with Whizard using a Standard Model and unit CKM matrix. No significant differences were observed, which indicates that enforcing a unit CKM matrix when generating the $\nu\nu$qqqq final state samples did not significantly affect this analysis.

2.4 Data Analysis

The following section contains a description of how the variables used throughout the anomalous gauge coupling sensitivity study are determined.

2.4.1 Limiting Beam Related Backgrounds

During the reconstruction, after the inner detector tracks have been reconstructed, the CLICTrackSelection processor is applied, which vetoes poorly reconstructed and fake tracks by applying simple quality cuts to the number of hits in the tracking sub-detectors. The CLICTrackSelection processors also reject tracks where the time of arrival at the calorimeter differs by more than 50 ns between a straight line of flight and a helix fit to the track. Applying this cut ensures that associations made between charged particles tracks and calorimetric energy deposits are consistent.

Following the reconstruction, the CLICPfoSelector processor is applied to remove reconstructed particle flow objects (PFOs) that originate from beam related backgrounds. This processor applies cuts on the p_T and timing information of the PFOs, which vary as a function of position in the detector and the PFO type to target regions of the detector where backgrounds are more prominent, e.g. low p_T for $\gamma\gamma \rightarrow hadrons$ events. Three configurations of the CLICPfoSelector have been developed for the CLIC environment and were considered in this analysis. They are, in order of increasing background rejection, the Loose, Default and Tight selections [25].

2.4.2 Jet Finding

After the application of the CLICPfoSelector, the MarlinFastJet processor, a wrapper for the FastJet [27] processor, was used to cluster each event into four jets. These jets are then paired up to form two candidate bosons working under the assumption that the correct pairing is achieved when the difference between the invariant masses of the candidate bosons is a minima. In the case of the signal final state, $\nu\nu$qqqq, it is assumed that the four jets and two candidate bosons map onto the four primary quarks and two outgoing bosons in the vector boson scattering process. The jet clustering was performed using the longitudinally invariant k_t jet algorithm in exclusive mode. The longitudinally invariant k_t algorithm proceeds as follows

1. Determine the k_t distance, d_{ij}, for each pair of particles, i and j, and the beam, d_{iB}, distance for each particle, i. These distances are defined as

$$d_{ij} = \min(p_{ti}^2, p_{tj}^2)\Delta R_{ij}^2 / R^2 \ , \tag{2.3}$$

$$d_{iB} = p_{ti}^2 \ , \tag{2.4}$$

where $\Delta R_{ij}^2 = (y_i - y_j)^2 + (\phi_i - \phi_j)^2$, p_{ti} is the transverse momentum of particle i, y_i is the rapidity of particle i, ϕ_i is the azimuthal angle of the direction of travel of particle i and R is a configurable parameter that typically is of the order of 1.

2. Find the minimum distance, $d_{\min}$, of all the k_t and beam distances. If the minimum occurs for a k_t distance, particles i and j are merged, summing their 4-momenta. If the beam distance is the minima, particle i was declared to be part of the "beam" jet and the particle is removed from the list of particles and not included in the final jet output.

3. Repeat until the desired number of jets is created. Alternatively, in inclusive mode this would be repeated until no particles are left in the event.

Two other clustering algorithms were considered, however, they were found to be inappropriate for the experimental conditions at CLIC. These alternative algorithm choices are applied in the same manner as the longitudinally invariant k_t algorithm, however, they differ in the definition of d_{ij} and d_{iB}. Figure 2.5 shows the distribution of the invariant mass of the candidate bosons for $\sqrt{s} = 1.4$ TeV $\nu\nu$qqqq final state events for each of the jet algorithms considered. The candidate boson masses are determined by forcing the events into 4 jets and then pairing the jet pairs to form candidate bosons. The jet pairing configuration is determined by pairing jets such that the mass differences between the two candidate bosons is a minimum.

The first alternative jet algorithm considered was the k_t algorithm for $\mathrm{e^+e^-}$ colliders, the $\mathrm{e^+e^-}$ k_t or Durham algorithm. In this algorithm d_{iB} is not used and

$$d_{ij} = 2\min(E_i^2, E_j^2)(1 - cos\theta_{ij}) \ , \tag{2.5}$$

where θ_{ij} is the opening angle of particles i and j and E_i is the energy of particle i. In the collinear limit d_{ij} corresponds to the relative transverse momenta of the particles. The major failure of this algorithm when applied to CLIC is the absence of d_{iB}, which leads to large numbers of beam related background particles being associated to jets. As figure 2.5 shows, the invariant mass of the paired jets, which should peak around
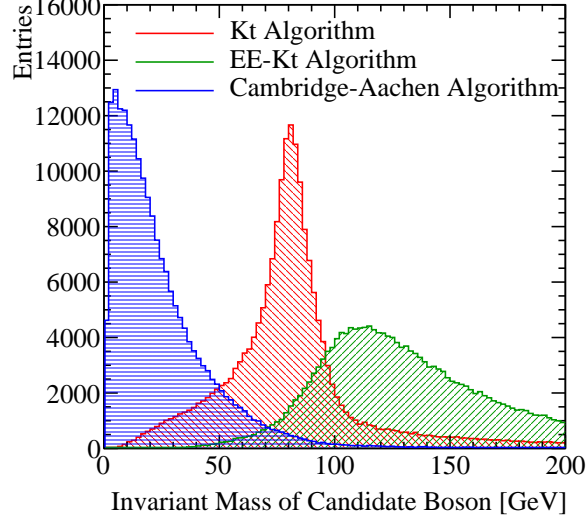
Figure 2.5: The reconstructed masses for different choices of jet algorithm for $\sqrt{s} = 1.4$ TeV
$\nu\nu$qqqq final state events. These samples should be dominated by vector boson
scattering involving pairs of outgoing W bosons and so it is expected that a peak
at the W boson mass, $m_W = 80.385 \pm 0.015$ GeV [15], should be observed. In
the case of the k_t algorithm and the $\mathrm{e^+e^-}\,k_t$ algorithm an R parameter of 0.7 was
used. All distributions show raw number of events.

the W and Z boson masses, is much larger than expected, due to the presence of these
backgrounds. Also this algorithm is not invariant to boosts along the beam direction
meaning that it is inappropriate for use at CLIC given the beam induced backgrounds
modify the nominal collision kinematics.

The second alternative jet algorithm considered was the Cambridge-Aachen jet
algorithm where

$$d_{ij} = \Delta R_{ij}^2 / R^2 \ , \tag{2.6}$$

$$d_{iB} = 1 \ . \tag{2.7}$$

This algorithm performs poorly as it does not account for the transverse momentum or
the energy of the particles being clustered. In essence, this is a cone clustering algorithm
with a cone radius defined through $\Delta R_{ij} = R$, which even for large R was found to
discard too much energy in the event to be useful for this analysis. This can be seen in
figure 2.5 where the invariant mass of the paired jets is much lower than expected. This
algorithm is appropriate for events that contain highly boosted jets, however, at CLIC
the jets are too disperse for this algorithm to be successful.

2.4.2.1 Optimal Jet Finding Algorithm

Optimisation of the jet finding procedure was performed on both the PFO selection and
the value of the R parameter used in the longitudinally invariant k_t algorithm. The
optimisation procedure involved performing the sensitivity study, described in section
2.6, using solely the $\nu\nu$qqqq signal final state. This methodology ensures that the
optimisation was done with respect to the physics of interest without having to perform
the jet reconstruction for the large number of background events for each jet algorithm
configuration considered.

Table 2.3 shows the one σ confidence limits on the measurement of α_4 and α_5 obtained
using the $\nu\nu$qqqq signal final state only at $\sqrt{s} = 1.4$ TeV for different jet algorithm
configurations. These confidence limits represent the idealised sensitivity of the CLIC
experiment to the anomalous gauge couplings. Once the effects of backgrounds and event
selection are included in the analysis, these confidence limits will increase in size.

| R Parameter | PFO Selection | | |
	Tight Selected PFOs	Selected PFOs	Loose Selected PFOs
0.7	$-0.0039 < \alpha_4 < 0.0051$	$-0.0035 < \alpha_4 < 0.0047$	$-0.0037 < \alpha_4 < 0.0047$
	$-0.0027 < \alpha_5 < 0.0031$	$-0.0025 < \alpha_5 < 0.0031$	$-0.0024 < \alpha_5 < 0.0028$
0.9	$-0.0036 < \alpha_4 < 0.0047$	$-0.0035 < \alpha_4 < 0.0045$	$-0.0035 < \alpha_4 < 0.0045$
	$-0.0026 < \alpha_5 < 0.0031$	$-0.0023 < \alpha_5 < 0.0027$	$-0.0022 < \alpha_5 < 0.0027$
1.1	$-0.0036 < \alpha_4 < 0.0047$	$-0.0036 < \alpha_4 < 0.0048$	$-0.0036 < \alpha_4 < 0.0046$
	$-0.0026 < \alpha_5 < 0.0031$	$-0.0025 < \alpha_5 < 0.0029$	$-0.0024 < \alpha_5 < 0.0028$

Table 2.3: One σ confidence limits on the measurement of α_4 and α_4 obtained using the $\nu\nu$qqqq
signal final state only at $\sqrt{s} = 1.4$ TeV for different jet algorithm configurations.

The configuration for the jet algorithm for the $\sqrt{s} = 1.4$ TeV analysis was chosen
as selected PFOs with an R parameter of 0.9. While the loose PFO selection gives a
marginally better performance, the selected PFO selection was preferred to minimise the
effects of the $\gamma\gamma \to hadrons$ background. Figure 2.6a shows confidence contours, given a
null hypothesis of $\alpha_4 = \alpha_5 = 0$, for the selected PFO and R parameter of 0.9 jet algorithm
configuration for $\sqrt{s} = 1.4$ TeV. Figures 2.6b and 2.6c show the one dimensional χ^2
distribution for α_4 and α_5, assuming $\alpha_5 = 0$ and $\alpha_4 = 0$ respectively, for the same
configuration.

(a)

(b)

(c)
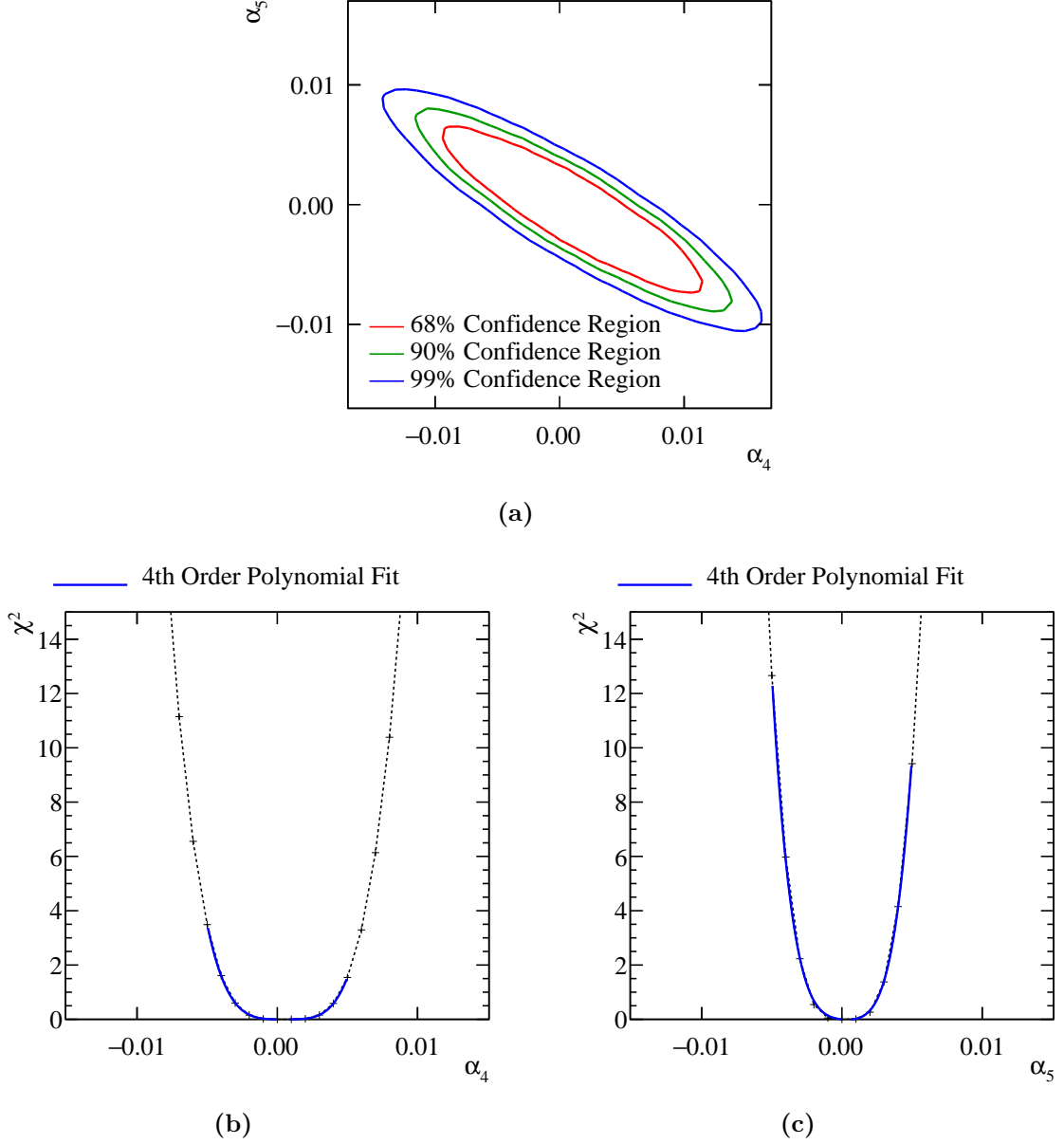
Figure 2.6: χ^2 sensitivity distributions from a fit to M_{VV} for the signal qqqq$\nu\nu$ final state only for $\sqrt{s} = 1.4$ TeV. These results use the optimal jet algorithm configuration of selected PFOs and an R parameter of 0.9 in the k_t algorithm. (a) χ^2 sensitivity contours in α_4 and α_5 space. (b) χ^2 as a function of α_4 assuming $\alpha_5 = 0$. (c) χ^2 as a function of α_5 assuming $\alpha_4 = 0$. All distributions are normalised to an integrated luminosity of $\mathcal{L}_{int} = 1.5$ ab^{-1}.

2.4.3 Lepton Finding

An isolated lepton finder [28] was included in the analysis chain to reject background final states containing primary leptons. Leptons produced via hadronisation are unlikely to be flagged as isolated because all hadronisation products are boosted along the direction of the parent quark. This means isolated leptons are likely to correspond to primary leptons, which makes the number of isolated leptons a powerful discriminating variable to use in event selection.

The isolated lepton finder determines whether a PFO is an electron or muon by first checking that the PFO has a single charged particle track associated to it. If that is the case, the calorimetric energy deposits of the PFO are examined to see if they are consistent with what is expected for an electron or muon. If they are consistent with expectations, the properties of the charged particle track are examined to determine whether the track originates from the IP. If the PFO is deemed to have originated from the IP, isolation checks, which examine the energy deposited in the calorimeters within a cone surrounding the PFO, are applied to determine whether the particles belongs to a jet. If the PFO does not appear to belong to a jet then it is counted as an isolated lepton. The fraction of events rejected by the lepton finder is summarised in table 2.4.

Final State	$\epsilon_{\text{Lepton Finding}}$
$e^+e^- \rightarrow \nu\nu qqqq$	99.7
$e^+e^- \rightarrow \nu l qqqq$	48.9

Table 2.4: The fraction of events rejected by of isolated lepton finding for $\sqrt{s} = 1.4$ TeV for the $\nu\nu qqqq$ and $l\nu qqqq$ final states.

2.4.4 Discriminant Variables

The next stage of the analysis involved the calculation of a number of event-based variables that were found to be useful for this analysis. The variables that were calculated are as follows

- **Particle level** variables:

  – Number of PFOs in each jet;

  – Energy of the highest energy PFO;

- Energy of the highest energy electron;

- Cosine of the polar angle of the highest energy track;

- The number of isolated leptons found using the isolated lepton finder.

- **Candidate boson** variables:

  - Energy of the candidate bosons;

  - Invariant mass of the candidate bosons;

  - Acolinearity of the candidate boson pair, which is defined as 180 degrees minus the opening angle of the pair of bosons in the rest frame of the detector.

- **Event based** variables:

  - The invariant mass of the visible system, M_{VV};

  - The vector sum of the transverse momentum of all PFOs in the event;

  - Sphericity, defined through the sphericity tensor S^{ab};

$$S^{ab} = \frac{\Sigma_i p_i^\alpha p_j^\alpha}{\Sigma_{i,\alpha=1,2,3}|p_i^\alpha|^2} \tag{2.8}$$

  Where p_i are the components of the momenta of PFO i in the rest frame of the detector and the sum Σ_i runs over all particles in the event. Sphericity is defined as $S = \frac{3}{2}(\lambda_2 + \lambda_3)$, where λ_i are the eigenvalues of the sphericity tensor defined such $\lambda_1 \geq \lambda_2 \geq \lambda_3$. This provides a measure of how spherical the reconstructed event topology is with isotropic events having $S \approx 1$, while two jet events have $S \approx 0$.

- **Jet clustering parameters** variables:

  - The y_{ij} variables where $i = 3, 4$ and $j = i + 1$. These are the smallest k_t distance found when combining j jets into i jets.

2.4.5 Jet Energy Resolution at CLIC

The importance of the jet energy resolution, which is extensively discussed in chapters **??** and **??**, should be emphasised at this point. Many of the discriminant variables that are calculated for this analysis are dependant upon the jet energy resolution. In particular,
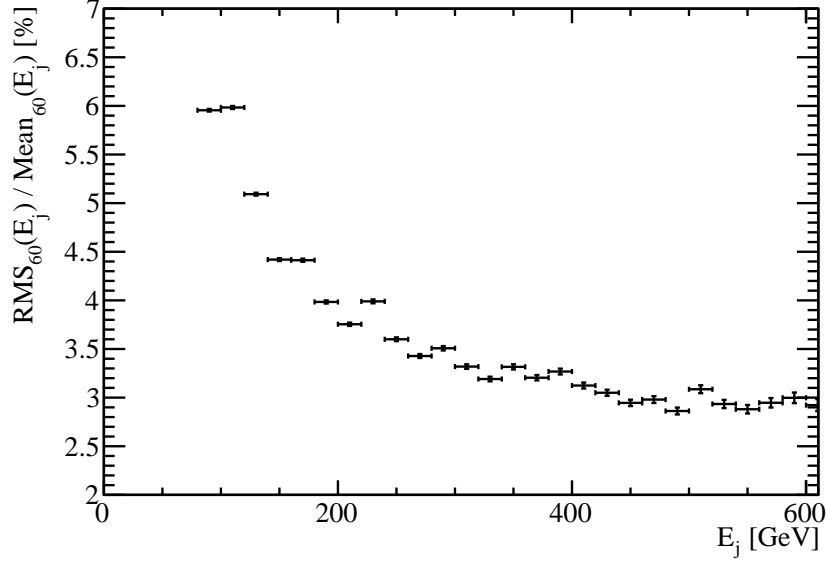
Figure 2.7: The jet energy resolution as a function of the jet energy for the $\nu\nu$qqqq final state for $\sqrt{s} = 1.4$ TeV.

all variables related to the candidate bosons that are formed from pairing up jets, are dependent upon the measurement of jet energies.

Figure 2.7 shows the jet energy resolution as a function of the MC jet energy for the $\nu\nu$qqqq event sample used in the $\sqrt{s} = 1.4$ TeV analysis. The MC jet energy was obtained by pairing up quarks appearing in the final state to the reconstructed jets. The events were then binned in terms of their MC jet energy and the jet energy resolution calculated for each bin. When calculating the jet energy resolution, a narrower range of jet energies was used in compared to previous studies, 60% of the data with narrowest RMS as opposed to 90%, to minimise the effects of jet finding and beam-induced backgrounds. The jet energy resolutions reported here are worse than those quoted in earlier chapters. This is to be expected given the effects of jet finding and beam-induced backgrounds.

2.5 Event Selection

This section discusses the event selection procedure. The goal of this procedure is to isolate the $\nu\nu$qqqq final state from the background final states, i.e. those containing two and four primary quarks. The procedure consists of a set of preselection cuts followed by the application of a multivariate analysis (MVA). All event numbers have

been normalised, prior to event selection, to an integrated luminosity of $\mathcal{L}_{int} = 1.5$ ab^{-1} for the $\sqrt{s} = 1.4$ TeV analysis and $\mathcal{L}_{int} = 2$ ab^{-1} for the $\sqrt{s} = 3$ TeV analysis.

2.5.1 Preselection

A refined selection of the $\nu\nu$qqqq signal final state is achieved using a MVA, however, to ensure efficiency in the training and application of that MVA a number of simple preselection cuts were developed to veto obvious background final states prior to the application of the MVA. Preselection cuts were applied to the transverse momentum of the system and the number of isolated leptons found in the event. The raw distributions of these variables is shown in figure 2.8 and based on these distributions the following cuts were applied

- Transverse momentum of system > 100 GeV. This cut is effective due to the presence of missing energy in the form of neutrinos in the signal final state.

- Number of isolated leptons in system $= 0$. This cut is effective as the signal final state does not contain leptons, while numerous background final states do.

The impact of these preselection cuts can be found in table 2.5, which can be found on page 58.

2.5.2 Multivariate analysis

Having established the preselection cuts, a MVA was applied using the TMVA toolkit [29], to refine the event selection. The signal and background final state samples were separated into two equally sized samples; one sample was used to independently train the MVA and the other sample was used in the subsequent analysis.

The performance of several MVA classifiers was examined to determine the optimal classifier for this analysis. The MVA classifiers considered were [29]:

- **Boosted Decision Tree (BDT)**. Decision trees are formed by the sequential application of cuts that split the data into multiple classes. After the application of the final cut, the remaining classes are used to classify whether the input event corresponds to signal or background. Boosting a decision tree involves the use of several decision trees. A single classifier output is obtained from a weighted average
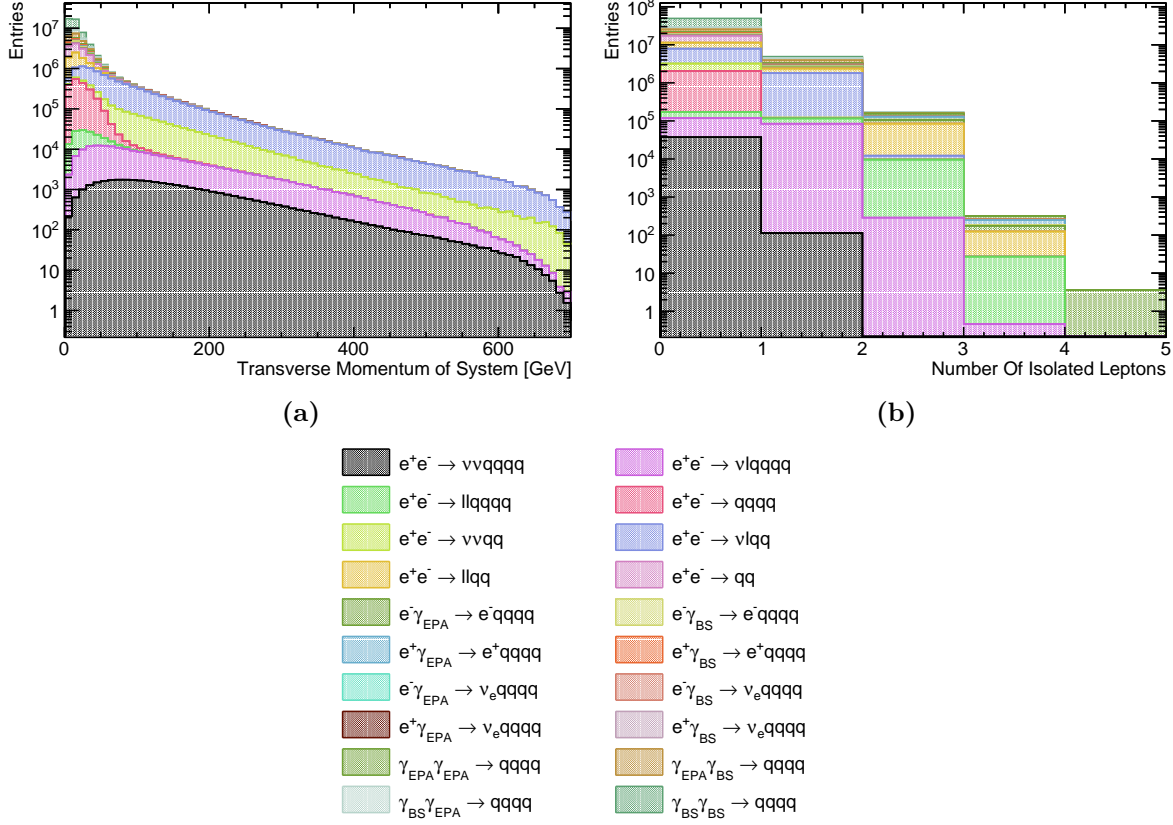
Figure 2.8: Distribution of the preselection cut variables for $\sqrt{s} = 1.4$ TeV: (a) the transverse
momentum of the visible system; and (b) the number of isolated leptons in
the system. All distributions are normalised to an integrated luminosity of
$\mathcal{L}_{int} = 1.5$ ab^{-1}.

of the individual decision trees. The cuts applied in the decision tree are determined
using the training sample.

- **k-Nearest Neighbour (KNN)**. For a given input event, the k closest neighbours
  from the training sample are found. The classifier for that input event is determined
  as the fraction of those k events that belong to the signal sample. Distances in this
  classifier are defined as the Euclidean distance between events in the n-dimensional
  space of the variables used for training the classifier. Weights are applied when
  calculating the distances to account for the differing widths of the input variable
  distributions. The value of k used in this analysis was 20.

- **Multilayer Perceptron (MLP)**. This is an example of a neutral network. Neutral
  networks consist of an interconnected series of neurons each with a different response
  to a set of input signals. The signal for the first layer of neurons in this case are

the event variables used to train the MVA. The input signal proceeds to travel through several layers of neurons. The number of neurons in a given layer is reduced as the number of layers passed through increases until two neurons are left, one corresponding to signal and the other background. The neuron giving the larger response in the final layer determines the event classifier. The training sample is used to determine the response of each neurons in the network.

- **Fisher and H-Matrix Discriminants**. These procedures involve the calculation of a hyperplane in n-dimensional space that maximally separates signal and background events in the training sample. The location of an input event in that n-dimensional space with respect to that hyperplane determines the classifier for the event. The hyperplane is determined by maximising the differences between the means of the input event variables normalised by a measure of their spread. Both the Fisher and H-Matrix discriminants search for the hyperplane in n-dimensional space, however, the Fisher discriminant begins this procedure by transforming the input variables into a variable space with zero linear correlations.

- **Likelihood**. The likelihood is determined using the probability density function (PDF) for each of the input variables. PDFs are determined using the training sample for both signal and background events. For a given event, the likelihood is given by the product of the probability of obtaining each of the input variables for that event. The signal and background likelihoods are calculated using the signal and background PDFs respectively and the ratio of the signal likelihood to the sum of the signal and background likelihoods gives the event classifier.

The input variables used for these MVA classifiers were:

- Number of PFOs in each jet;

- Energy of the highest energy PFO;

- Energy of the highest energy electron;

- Cosine of the polar angle of the highest energy track;

- Energy of the candidate bosons;

- Invariant mass of the candidate bosons;

- Acolinearity of the candidate boson pair;

- The vector sum of the transverse momentum of all PFOs in the event;
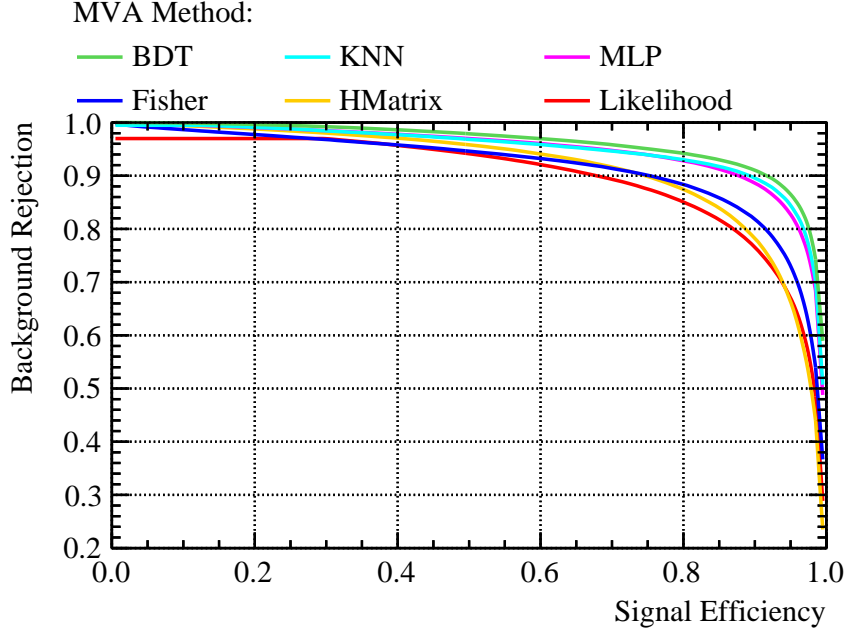
Figure 2.9: Background rejection as a function of signal efficiency for a variety of MVA options for $\sqrt{s} = 1.4$ TeV.

- The sphericity of the event;

- The derived jet clustering parameter variables $-\log_{10}(y_{ij})$ where y_{ij} are jet clustering parameters, $i = 3, 4$ and $j = i + 1$.

Figure 2.9 shows the background rejection, which is equivalent to one minus the background efficiency, as a function of signal efficiency for various MVA classifiers. Efficiency is defined as the fraction of events classified as signal by the MVA. The efficiencies reported by TMVA are calculated after the application of the preselection cuts, which are described in section 2.5.1.

The classifier giving the optimal performance in terms of signal efficiency and background rejection was the BDT. The performance of the BDT was optimised further by varying the number of trees used and the depth of the trees. An optimal significance, $S/\sqrt{(S + B)}$, where S and B are the number of signal and background events passing the preselection respectively, of 52.7 was obtained using the optimised BDT.

2.5.3 Event Selection Summary

The event selection is summarised using the distribution of the invariant mass of the candidate bosons, which for the signal final state should peak around the W mass. This distribution is shown in figure 2.10 with: no event selection; with the preselection cuts applied; and with both preselections cuts and MVA applied. The event selection efficiencies are also summarised in table 2.5.

As expected the dominant background processes after the MVA is applied are those that have the same topology as the signal process, i.e. four primary quarks with missing energy. Two smaller sources of background are also present: two jet events with missing energy that are confused with four jet events with missing energy and events where a lepton is not properly reconstructed causing the event to look like four jets and missing energy.

2.6 Anomalous Coupling Fitting Methodology

This section describes the procedure used for constructing the χ^2 surface and the subsequent confidence contours used to determine the sensitivity of CLIC to the anomalous gauge couplings α_4 and α_5.

2.6.1 Sensitive Distribution

The sensitivity of CLIC to the anomalous gauge couplings will be determined through the use of a χ^2 fit. Three variables showing sensitivity to the anomalous gauge couplings were considered for use in the χ^2 fit:

- M_{VV}. The invariant mass of the visible system;

- $\cos\theta^*_{Bosons}$. The angle between the boost direction and the back-to-back candidate bosons in the rest frame of the visible system;

- $\cos\theta^*_{Jets}$. The angle between the boost direction and the back-to-back jets in the rest frame of the candidate bosons. As each event contains two candidate bosons, there are two $\cos\theta^*_{Jets}$ variables per event.

(a)

(b)

(c)
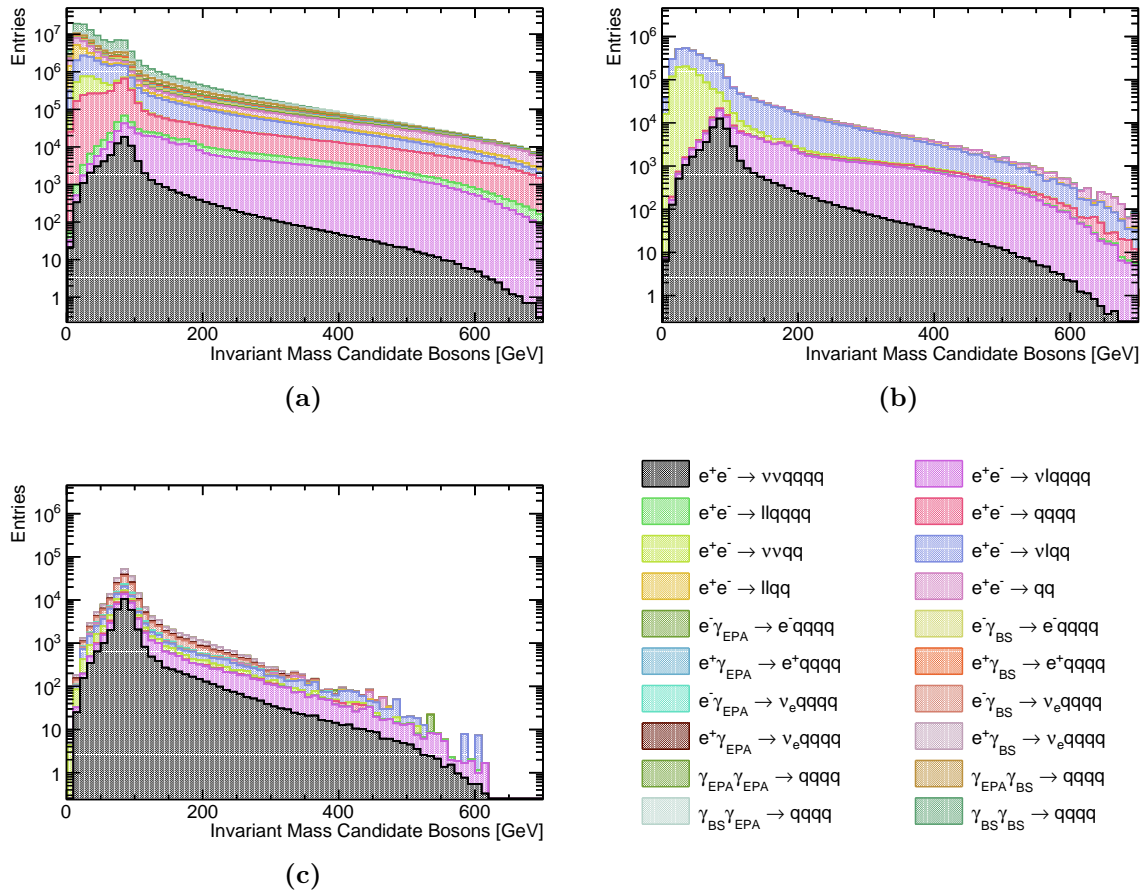
Figure 2.10: Impact of preselection and MVA on the reconstructed invariant mass of the candidate bosons for $\sqrt{s} = 1.4$ TeV: (a) no cuts; (b) after preselection; and (c) after preselection and MVA. All distributions correspond to an integrated luminosity of $\mathcal{L}_{int} = 1.5$ ab^{-1}.

Final State	ϵ_{presel}	ϵ_{BDT}	N_{BDT}
$e^+e^- \to \nu\nu qqqq$	64.1%	44.5%	16,470
$e^+e^- \to \nu lqqqq$	26.1%	5.2%	8,582
$e^+e^- \to llqqqq$	0.8%	0.1%	100
$e^+e^- \to qqqq$	0.3%	0.1%	1,698
$e^+e^- \to \nu\nu qq$	43.4%	0.5%	5,351
$e^+e^- \to \nu lqq$	19.1%	0.1%	9,319
$e^+e^- \to llqq$	0.1%	-	234
$e^+e^- \to qq$	0.6%	-	1,586
$e^-\gamma_{\text{EPA}} \to e^- qqqq$	0.2%	-	48
$e^-\gamma_{\text{BS}} \to e^- qqqq$	0.1%	-	42
$e^+\gamma_{\text{EPA}} \to e^+ qqqq$	0.3%	-	19
$e^+\gamma_{\text{BS}} \to e^+ qqqq$	-	-	65
$e^-\gamma_{\text{EPA}} \to \nu_e qqqq$	26.0%	9.0%	4,421
$e^-\gamma_{\text{BS}} \to \nu_e qqqq$	36.1%	15.0%	23,150
$e^+\gamma_{\text{EPA}} \to \overline{\nu}_e qqqq$	25.9%	9.2%	4,495
$e^+\gamma_{\text{BS}} \to \overline{\nu}_e qqqq$	36.4%	15.3%	23,410
$\gamma_{\text{EPA}}\gamma_{\text{EPA}} \to qqqq$	0.2%	-	81
$\gamma_{\text{EPA}}\gamma_{\text{BS}} \to qqqq$	0.1%	-	55
$\gamma_{\text{BS}}\gamma_{\text{EPA}} \to qqqq$	-	-	53
$\gamma_{\text{BS}}\gamma_{\text{BS}} \to qqqq$	-	-	0

Table 2.5: Event selection efficiencies for $\sqrt{s} = 1.4$ TeV. In the above table, ϵ_{presel} denotes the number of events passing the preselection as a fraction of the total number of events, while ϵ_{BDT} denotes the number of events passing both the preselection and the BDT as a fraction of the total number of events. The EPA and BS subscript on the incoming photon indicates whether the photon is generated from the equivalent photon approximation or beamstrahlung. Entries with a dash indicate an efficiency of less than 0.1%. The event numbers correspond to an integrated luminosity of $\mathcal{L}_{int} = 1.5$ ab^{-1}.

Figure 2.11 shows the distribution of these variables for the $\nu\nu qqqq$ final state for selected values of the anomalous gauge couplings α_4 and α_5. A χ^2 fit to each of these variables was applied to obtain confidence limits on the sensitivity of CLIC to the anomalous gauge couplings, as described in section 2.6.2. The distributions used for the χ^2 fit contained signal and background events that passed event selection. Table 2.6 shows the one σ confidence limits on the measurement of α_4 and α_5 obtained using

each of the variables considered. The M_{VV} distribution shows the greatest sensitive to the anomalous gauge couplings; therefore, it will be used by all subsequent χ^2 fits when reporting sensitivities. This distribution shows the greatest sensitivity of the variables considered because the couplings primarily affect events with large values of M_{VV} and there are relatively few of these events.

Sensitive Variable	One σ Confidence Limits
M_{VV}	$-0.0082 < \alpha_4 < 0.0116$
	$-0.0055 < \alpha_5 < 0.0078$
$\cos\theta^*_{Bosons}$	$-0.0111 < \alpha_4 < 0.0155$
	$-0.0082 < \alpha_5 < 0.0110$
$\cos\theta^*_{Jets}$	$-0.0100 < \alpha_4 < 0.0142$
	$-0.0070 < \alpha_5 < 0.0098$

Table 2.6: One σ confidence limits on the measurement of α_4 and α_5 obtained at $\sqrt{s} = 1.4$ TeV. These sensitivities include the affect from backgrounds and event selection.

2.6.2 χ^2 Surface and Confidence Limit Definition

A χ^2 surface was used to determine confidence limits on the anomalous gauge couplings given the null hypothesis that $\alpha_4 = \alpha_5 = 0$. This surface is defined as

$$\chi^2 = \sum_i \frac{(O_i - E_i)^2}{E_i}, \tag{2.9}$$

where O_i is the observed, $\alpha_4 = \alpha_5 = 0$, and E_i the expected, $\alpha_4 \neq 0$ and $\alpha_5 \neq 0$, bin content for bin i in the distribution of interest. The summation Σ_i runs over bins in the distribution of interest.

When applying the χ^2 fit to the M_{VV} distribution, the distribution was binned using 13 bins as shown in figure 2.12. The first bin spanned the invariant mass range between 0 GeV and 200 GeV, this was followed by 11 bins of width 100 GeV ranging from 200 GeV to 1300 GeV and finally the last bin contained all invariant masses above 1300 GeV. The expanded bin widths at the tails of the distribution were chosen to ensure the bin contents were sufficiently large to give a reliable estimate the likelihood function using the χ^2 parameter. This choice of bin width also ensured the bin contents were sufficiently large to minimise fluctuations arising from individual events with large weights. When applying

(a)

(b)

(c)
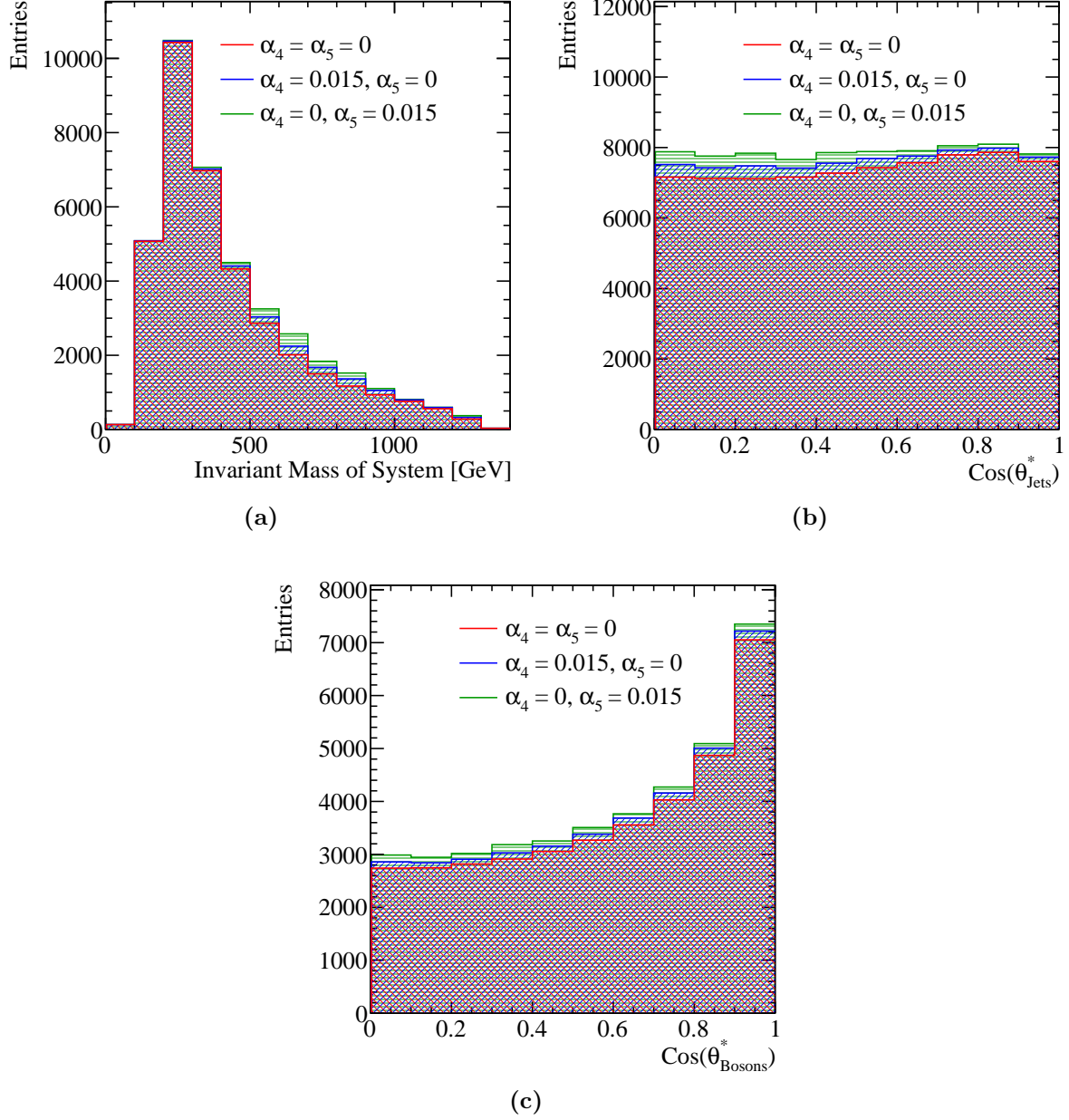
Figure 2.11: The distributions of (a) M_{VV}, (b) $\cos\theta^*_{Jets}$ and (c) $\cos\theta^*_{Bosons}$ for selected values of the anomalous gauge couplings α_4 and α_5 for the $\nu\nu$qqqq final state for $\sqrt{s} = 1.4$ TeV. The jet algorithm used was the longitudinally invariant k_t algorithm with an R parameter of 0.9 and Selected PFOs. All distributions are normalised to an integrated luminosity of $\mathcal{L}_{int} = 1.5$ ab^{-1}.

the χ^2 fit to distributions of the $\cos\theta^*_{Bosons}$ and $\cos\theta^*_{Jets}$ variables, the distributions were binned using 10 bins ranging from zero to one. As there are two $\cos\theta^*_{Jets}$ variables per event, the χ^2 fit was applied to a two dimensional distribution of $\cos\theta^*_{Jets}$, where

a distinction between the two $\cos\theta^*_{Jets}$ variables was made based on the energy of the candidate bosons. The use of a two dimensional distribution in the χ^2 fit was needed to account for any correlation between the two $\cos\theta^*_{Jets}$ variables.

Confidence limits describing the sensitivity of the CLIC experiment to the anomalous gauge couplings were found by examining the χ^2 surface in the space of α_4 and α_5. Deviations from the minima of this surface, which by construction occurs at $\alpha_4 = \alpha_5 = 0$, yield confidence limits that indicate the probability of observing a particular value of α_4 and α_5 given the null hypothesis that $\alpha_4 = \alpha_5 = 0$. The confidence limits reported in subsequent sections, 68%, 90% and 99%, are defined using fixed deviations from the minima of χ^2 surface ($\Delta\chi^2$) of 2.28, 4.61 and 9.21 respectively.

Confidence limits on the individual parameters α_4 and α_5 were determined by setting the corresponding coupling term to zero and examining the remaining one dimensional χ^2 distribution. A fourth order polynomial was fitted to the minima of this distribution and the one sigma confidence limit defined using $\Delta\chi^2 = 1$. The definition of a one sigma confidence limit accounts for changes in the number of degrees of freedom in the fit, therefore, it changes when fixing the corresponding coupling term to zero.
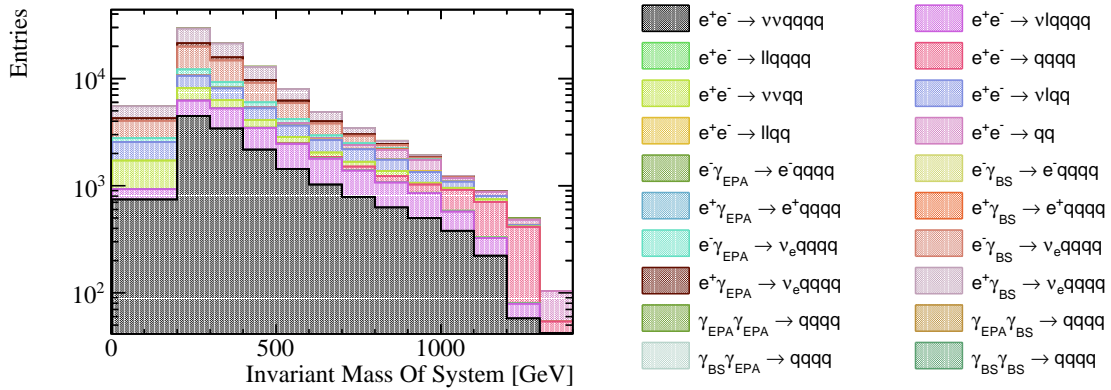
Figure 2.12: The distribution of the invariant mass of the system for both signal and background finals states that is used in the χ^2 fit for $\sqrt{s} = 1.4$ TeV. The distribution includes effect of event selection and corresponds to an integrated luminosity of $\mathcal{L}_{int} = 1.5$ ab^{-1}.

2.6.3 Event Weight Interpolation Scheme

In order to obtain a smooth χ^2 surface a fine sampling of the event weights in the α_4 and α_5 space is required, however, it is unfeasible to generate a finely sampled grid of event

weights on an event by event basis because event generation is highly CPU intensive. To resolve this issue, an interpolation scheme was applied to determine the event weights within a sampled region of the α_4 and α_5 space. This allows for an infinite sampling of the event weights in the space of α_4 and α_5 without having to call the generator an infinite number of times.

A bicubic interpolation scheme, cubic interpolation along the two dimensions, was applied to the event weights produced by the generator. This procedure is best illustrated by figure 2.13, which shows the interpolated event weight surface superimposed with the raw event weights from the generator for four $\nu\nu$qqqq events for $\sqrt{s} = 1.4$ TeV. This interpolation scheme produces a smooth and continuous surface that can be used for generating a smooth χ^2 surface.

2.7 Results

The sensitivity of the CLIC experiment to the anomalous gauge couplings α_4 and α_5 for $\sqrt{s} = 1.4$ TeV is shown in figure 2.14a. This result shows the sensitivity after the application of preselection and MVA purposed to remove the included background channels. These contours yield the one σ confidence limits for CLIC operating for $\sqrt{s} = 1.4$ TeV of

$$-0.0082 < \alpha_4 < 0.0116, \tag{2.10}$$

$$-0.0055 < \alpha_5 < 0.0078. \tag{2.11}$$

2.7.1 Systematic Uncertainties

A source of systematic error in this experiment is the uncertainty on the cross-sections for the signal and background processes. Based on the event selection summary shown in table 2.5, the dominant source of background in this analysis comes from the $e^{\pm}\gamma_{BS} \rightarrow \nu_e$qqqq processes. Therefore, uncertainties on the cross-section for these processes, as well as the signal process $e^+e^- \rightarrow \nu\nu$qqqq, will be considered.

The uncertainty on the cross-section for a given process is included in the χ^2 definition through the use of a nuisance parameter. This procedure allows the cross-section for a process to fluctuate, however, the magnitude of the fluctuation, r, is moderated by an

(a)

(b)

(c)

(d)
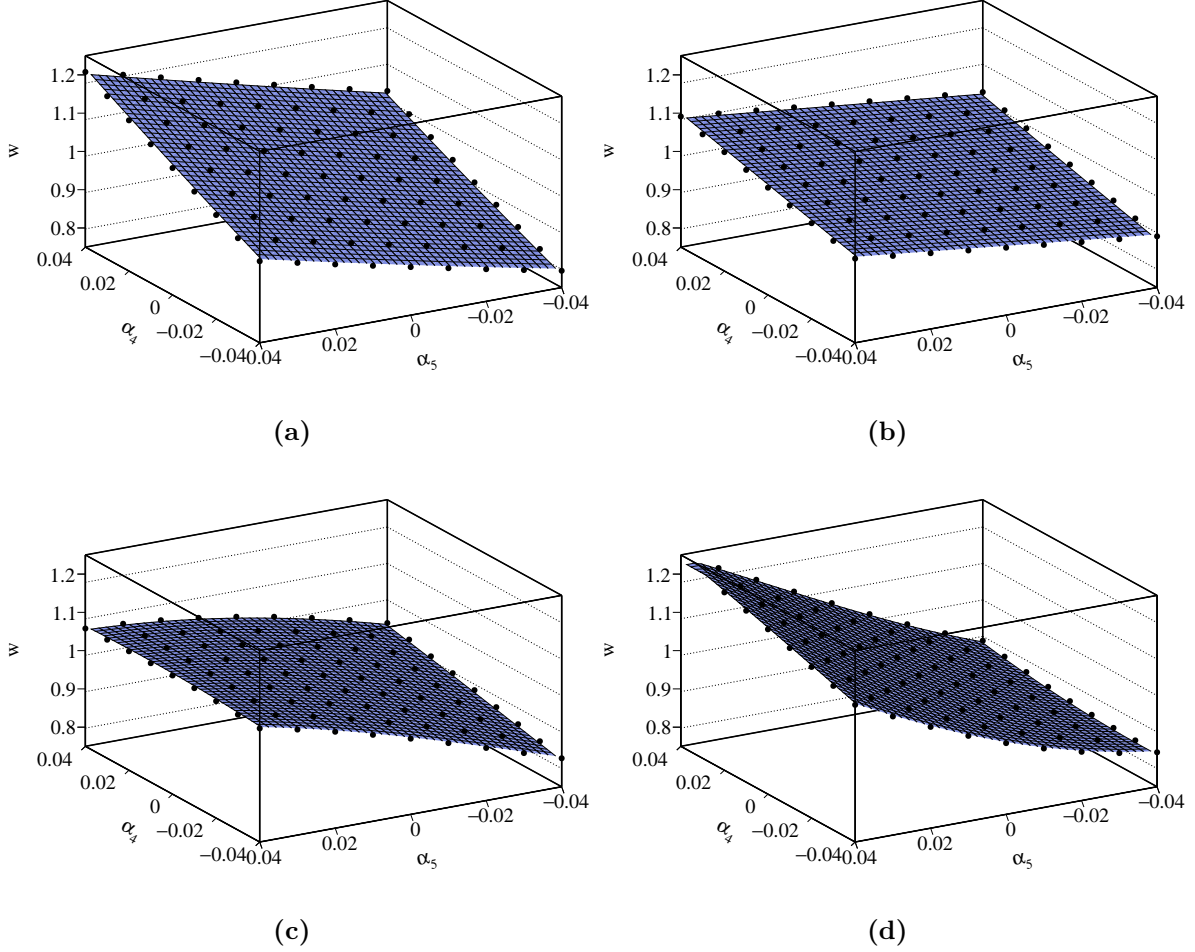
Figure 2.13: The event weight, w, as a function of the anomalous couplings α_4 and α_5 for a selection of $\sqrt{s} = 1.4$ TeV $\nu\nu$qqqq final state events. The black circles show the event weight produced from the generator and the blue surface is determined using bicubic interpolation between these points.

additional penalty term in the χ^2 as follows

$$\chi^2(r) = \sum_i \frac{(O_i - E_i(r))^2}{E_i(r)} + \frac{(r-1)^2}{\sigma_r^2}, \qquad (2.12)$$

where O_i is the observed, $\alpha_4 = \alpha_5 = 0$, bin content for bin i in the distribution of M_{VV} with no background fluctuations and $E_i(r)$ is the expected, $\alpha_4 \neq 0$ and $\alpha_5 \neq 0$, bin content for bin i in the distribution of M_{VV} where the cross-section for the process of interest has been fluctuated by the factor r. The sum $\sum_i$ runs over the bins in the M_{VV} distribution. The σ_r variable is the width of the distribution of r, which indicates

(a)

(b)

(c)
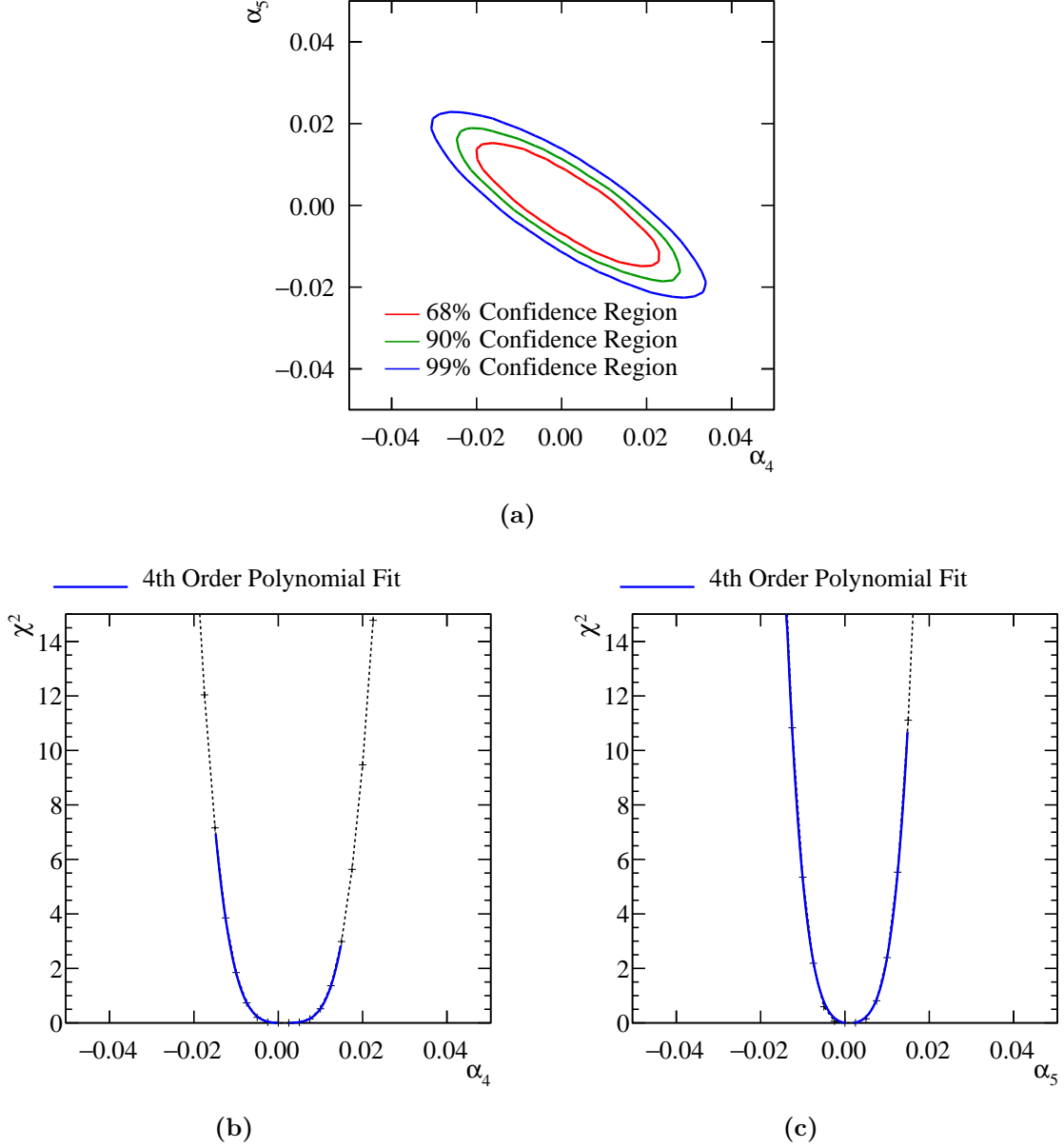
Figure 2.14: χ^2 sensitivity distributions from a fit to M_{VV} for $\sqrt{s} = 1.4$ TeV. Results include
the effect of backgrounds after the application of a series of preselection cuts
and MVA. (a) χ^2 sensitivity contours in α_4 and α_5 space. (b) χ^2 as a function
of α_4 assuming $\alpha_5 = 0$. (c) χ^2 as a function of α_5 assuming $\alpha_4 = 0$.

the uncertainty on the measurement of the cross-section of interest. A χ^2 surface is
constructed in the space of α_4 and α_5 by minimising $\chi^2(r)$ at each point.

The 68% confidence region is shown with the inclusion of a nuisance parameter for the
signal process $e^+e^- \to \nu\nu qqqq$ and the dominant background processes $e^\pm \gamma_{BS} \to \nu_e qqqq$

in figures 2.15a and 2.15b respectively. Minimal changes in sensitivity are observed when allowing the signal and dominant backgrounds to fluctuate. This can be understood by considering the shape of the M_{VV} distribution for the signal and dominant background processes, which is shown in figure 2.16. These distribution shows that anomalous couplings primarily affect events with large invariant masses, while both the signal and dominant backgrounds peak at low invariant masses. Therefore, by fluctuating the cross-section for the signal and dominant background processes, it is not possible to gain a significantly better match between the observed and expected bin contents in the M_{VV} distribution. This is encouraging as despite the $e^{\pm}\gamma_{BS} \to \nu_e qqqq$ backgrounds dominating the χ^2 fit that determines the sensitivity of CLIC to the anomalous gauge couplings, precise knowledge of their cross-section is not crucial. As the uncertainty on these cross-sections does not significantly affect the confidence regions, no cross-section uncertainties are accounted for when reporting the sensitivity of CLIC to the anomalous gauge couplings elsewhere in this analysis.

(a)   (b)
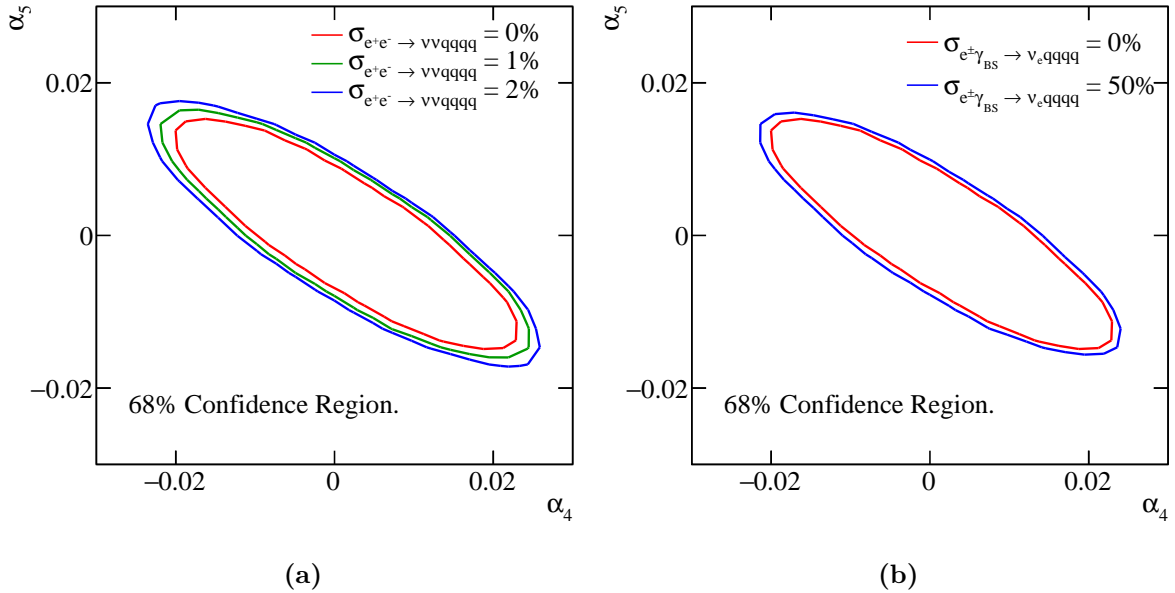
Figure 2.15: The 68% confidence region including the effect of uncertainties in the cross-section for (a) the signal process $e^+e^- \to \nu\nu qqqq$ and (b) the dominant background processes $e^{\pm}\gamma_{BS} \to \nu_e qqqq$.
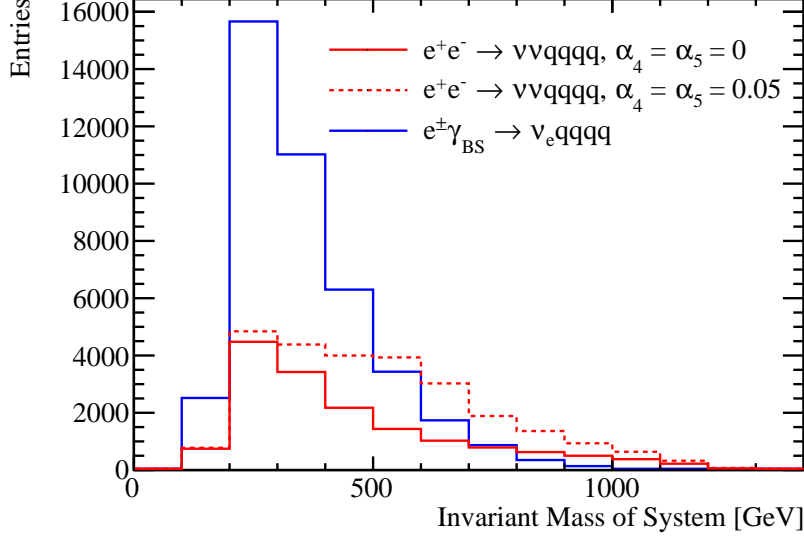
Figure 2.16: Distributions of M_{VV} for the $\mathrm{e^+e^-} \to \nu\nu$qqqq signal process, with and without
the effect from anomalous couplings, and the combined dominant background
processes $\mathrm{e^\pm}\gamma_{\mathrm{BS}} \to \nu_\mathrm{e}$qqqq. All distributions include the effect of event selection
and correspond to an integrated luminosity of $\mathcal{L}_{int} = 1.5$ ab^{-1}.

2.8 Sensitivity for $\sqrt{s} = 3$ TeV

The anomalous gauge coupling sensitivity study described in this chapter was repeated for
CLIC operating for $\sqrt{s} = 3$ TeV. As this analysis largely mirrors that of the $\sqrt{s} = 1.4$ TeV
analysis, this section focuses on the differences between the two analyses.

The signal and background final states for the $\sqrt{s} = 3$ TeV analysis were identical
to those used for the $\sqrt{s} = 1.4$ TeV analysis. Cross sections for these processes for
$\sqrt{s} = 3$ TeV are given in table 2.7. The data analysis and event selection procedures
used for $\sqrt{s} = 3$ TeV mirrored those used for $\sqrt{s} = 1.4$ TeV.

Jet finding was performed using the longitudinally invariant k_t algorithm as described
in section 2.4.2. The jet algorithm configuration was optimised using the sensitivity of
CLIC to the anomalous gauge couplings using pure signal only, as described in section
2.4.2.1. The optimal jet algorithm configuration for $\sqrt{s} = 3$ TeV used tight selected
PFOs and an R parameter of 1.1. As the cross-section for the $\gamma\gamma \to hadrons$ increases
with energy, the effect of these background is more problematic for $\sqrt{s} = 3$ TeV than for
$\sqrt{s} = 1.4$ TeV [25]. Therefore, it is to be expected that the optimal PFO selection for

Final State	Cross Section [fb]
$e^+e^- \to \nu\nu qqqq$	71.5
$e^+e^- \to \nu lqqqq$	106.6
$e^+e^- \to llqqqq$	169.3
$e^+e^- \to qqqq$	546.5
$e^+e^- \to \nu\nu qq$	1317.5
$e^+e^- \to \nu lqq$	5560.9
$e^+e^- \to llqq$	3319.6
$e^+e^- \to qq$	2948.9
$e^-\gamma_{EPA} \to e^- qqqq$	287.8
$e^-\gamma_{BS} \to e^- qqqq$	1268.6
$e^+\gamma_{EPA} \to e^+ qqqq$	287.8
$e^+\gamma_{BS} \to e^+ qqqq$	1267.3
$e^-\gamma_{EPA} \to \nu_e qqqq$	54.2
$e^-\gamma_{BS} \to \nu_e qqqq$	262.5
$e^+\gamma_{EPA} \to \overline{\nu}_e qqqq$	54.2
$e^+\gamma_{BS} \to \overline{\nu}_e qqqq$	262.3
$\gamma_{EPA}\gamma_{EPA} \to qqqq$	402.7
$\gamma_{EPA}\gamma_{BS} \to qqqq$	2423.1
$\gamma_{BS}\gamma_{EPA} \to qqqq$	2420.6
$\gamma_{BS}\gamma_{BS} \to qqqq$	13050.3

Table 2.7: Cross sections of signal and background processes for $\sqrt{s} = 3$ TeV. In the above table q represents u, $\overline{u}$, d, $\overline{d}$, s, $\overline{s}$, c, $\overline{c}$, b or $\overline{b}$; l represents $e^{\pm}$, $\mu^{\pm}$ or $\tau^{\pm}$; and ν represents ν_e, $\overline{\nu}_e$, ν_μ, $\overline{\nu}_\mu$, ν_τ and $\overline{\nu}_\tau$. The EPA and BS subscript on the incoming photon indicates whether the photon is generated from the equivalent photon approximation or beamstrahlung.

$\sqrt{s} = 3$ TeV, tight selected PFOs, is more aggressive at vetoing these backgrounds than for $\sqrt{s} = 1.4$ TeV, selected PFOs, which is what is observed.

As opposed to training the MVA using 50% of the signal and background events, as was done for the $\sqrt{s} = 1.4$ TeV analysis, the $\sqrt{s} = 3$ TeV analysis trained the MVA using 10% of the signal and background events. This modification prevented those events with very large event weights from dominating the χ^2 fit and producing exaggerated sensitivities. The sensitivity to the anomalous gauge couplings grows with increasing centre of mass energy, therefore, for $\sqrt{s} = 1.4$ TeV very large event weights were not an

issue. The sample sizes for all signal and background processes was sufficiently large that training on 10% of the total sample was sufficient to achieve good MVA performance. Event selection for the $\sqrt{s} = 3$ TeV analysis is summarised in table 2.8.

Final State	ϵ_{presel}	ϵ_{BDT}	N_{BDT}
$e^+e^- \to \nu\nu qqqq$	74.4%	46.0%	65,740
$e^+e^- \to \nu l qqqq$	40.0%	12.0%	25,660
$e^+e^- \to ll qqqq$	7.5%	1.1%	3,570
$e^+e^- \to qqqq$	3.7%	0.3%	3,224
$e^+e^- \to \nu\nu qq$	50.5%	1.2%	30,510
$e^+e^- \to \nu l qq$	32.0%	0.4%	48,320
$e^+e^- \to ll qq$	1.4%	-	1,028
$e^+e^- \to qq$	1.4%	0.1%	3,268
$e^-\gamma_{\text{EPA}} \to e^- qqqq$	6.6%	0.8%	4,736
$e^-\gamma_{\text{BS}} \to e^- qqqq$	4.6%	0.7%	13,660
$e^+\gamma_{\text{EPA}} \to e^+ qqqq$	6.5%	0.8%	4,686
$e^+\gamma_{\text{BS}} \to e^+ qqqq$	4.7%	0.7%	13,310
$e^-\gamma_{\text{EPA}} \to \nu_e qqqq$	45.6%	17.2%	18,610
$e^-\gamma_{\text{BS}} \to \nu_e qqqq$	55.9%	26.7%	110,900
$e^+\gamma_{\text{EPA}} \to \overline{\nu}_e qqqq$	45.9%	17.3%	18,750
$e^+\gamma_{\text{BS}} \to \overline{\nu}_e qqqq$	56.5%	27.4%	113,700
$\gamma_{\text{EPA}}\gamma_{\text{EPA}} \to qqqq$	5.3%	0.7%	5,531
$\gamma_{\text{EPA}}\gamma_{\text{BS}} \to qqqq$	3.5%	0.4%	16,640
$\gamma_{\text{BS}}\gamma_{\text{EPA}} \to qqqq$	3.5%	0.4%	15,900
$\gamma_{\text{BS}}\gamma_{\text{BS}} \to qqqq$	0.6%	-	4,124

Table 2.8: Event selection efficiencies for $\sqrt{s} = 3$ TeV. In the above table, ϵ_{presel} denotes the number of events passing the preselection as a fraction of the total number of events, while ϵ_{BDT} denotes the number of events passing both the preselection and the BDT as a fraction of the total number of events. The EPA and BS subscript on the incoming photon indicates whether the photon is generated from the equivalent photon approximation or beamstrahlung. Entries with a dash indicate an efficiency of less than 0.1%. The event numbers correspond to an integrated luminosity of $\mathcal{L}_{int} = 2$ ab^{-1}.

Due to the increased sensitivity of the signal sample, event weights were sampled with greater frequency in the space of α_4 and α_5 for $\sqrt{s} = 3$ TeV than for $\sqrt{s} = 1.4$ TeV analysis. Bicubic interpolation was again used to make a continuous surface for the event

weights. These event weight surfaces were then used to construct the M_{VV} distribution and the χ^2 surface used to determine the reported sensitivities. Figure 2.17 shows an example of the event weights extracted from the generator and the interpolated surface used to define the χ^2 surface as a function of α_4 and α_5 for a selected $\nu\nu qqqq$ event for $\sqrt{s} = 3$ TeV.


      (a)   **(b)**
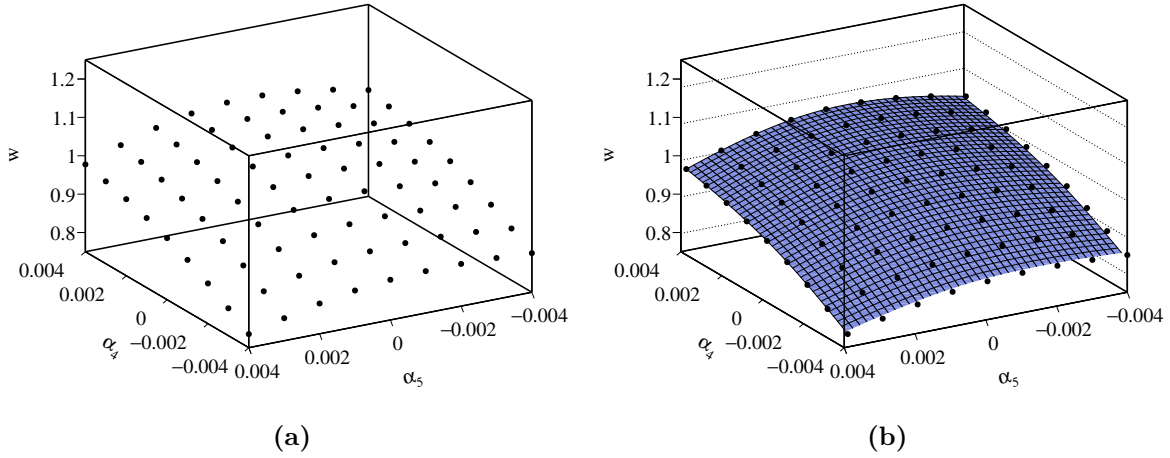
Figure 2.17: The event weights, w, as a function of the anomalous couplings α_4 and α_5 for a selected $\nu\nu qqqq$ final state events for $\sqrt{s} = 3$ TeV. These weights are calculated using (a) the generator and (b) bicubic interpolation.

A χ^2 was applied to the distribution of M_{VV} to determine the sensitivity of CLIC to the anomalous gauge couplings α_4 and α_5 for $\sqrt{s} = 3$ TeV. The M_{VV} distribution used for the fit had an increased number of bins with respect to the $\sqrt{s} = 1.4$ TeV analysis; the first bin spanned the invariant mass range between 0 GeV and 200 GeV, this was followed by 27 bins of width 100 GeV ranging from 200 GeV to 1300 GeV and finally the last bin contained all invariant masses above 2900 GeV. Figure 2.18 shows the M_{VV} distribution for signal and background processes for $\sqrt{s} = 3$ TeV that was used in the χ^2 fit.

The sensitivity of the CLIC experiment to the anomalous gauge couplings α_4 and α_5 for $\sqrt{s} = 3$ TeV is shown in figure 2.19a. This result shows the sensitivity after the application of preselection and MVA, described in sections 2.5.1 and 2.5.2, purposed to remove the included background channels. These contours yield the one σ confidence limit on the measurement of

$$-0.0010 < \alpha_4 < 0.0011, \tag{2.13}$$

$$-0.0007 < \alpha_5 < 0.0007. \tag{2.14}$$
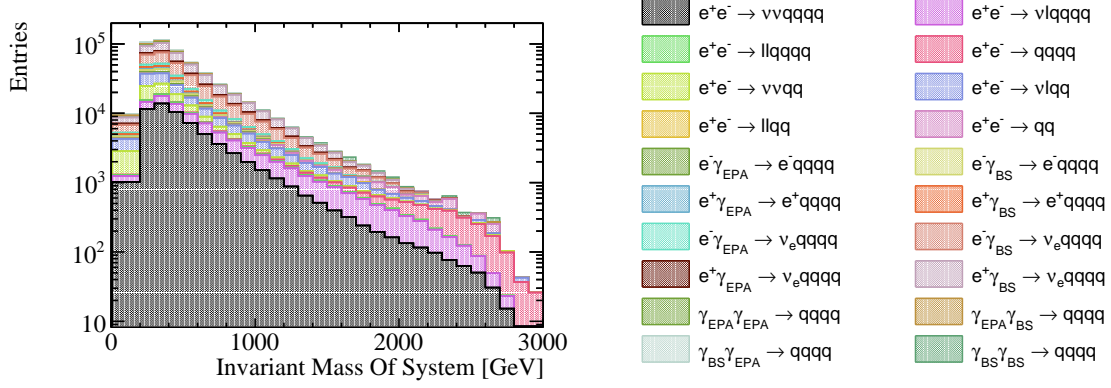
Figure 2.18: The distribution of the invariant mass of the system for both signal and background finals states that is used in the χ^2 fit for $\sqrt{s} = 3$ TeV. The distribution includes effect of event selection and corresponds to an integrated luminosity of $\mathcal{L}_{int} = 2$ ab^{-1}.

Figure 2.20 shows how the 68% confidence region for the $\sqrt{s} = 3$ TeV analysis varies with the uncertainty in the cross-section for the signal, $e^+e^- \rightarrow \nu\nu qqqq$, and dominant background processes, $e^{\pm}\gamma_{BS} \rightarrow \nu_e qqqq$. These contours were produced using a nuisance parameter as discussed in section 2.7.1. Once again, these systematic uncertainties have a small effect on the reported sensitivity of CLIC to the anomalous gauge couplings due to the shape of the M_{VV} distribution.

(a)

(b)

(c)
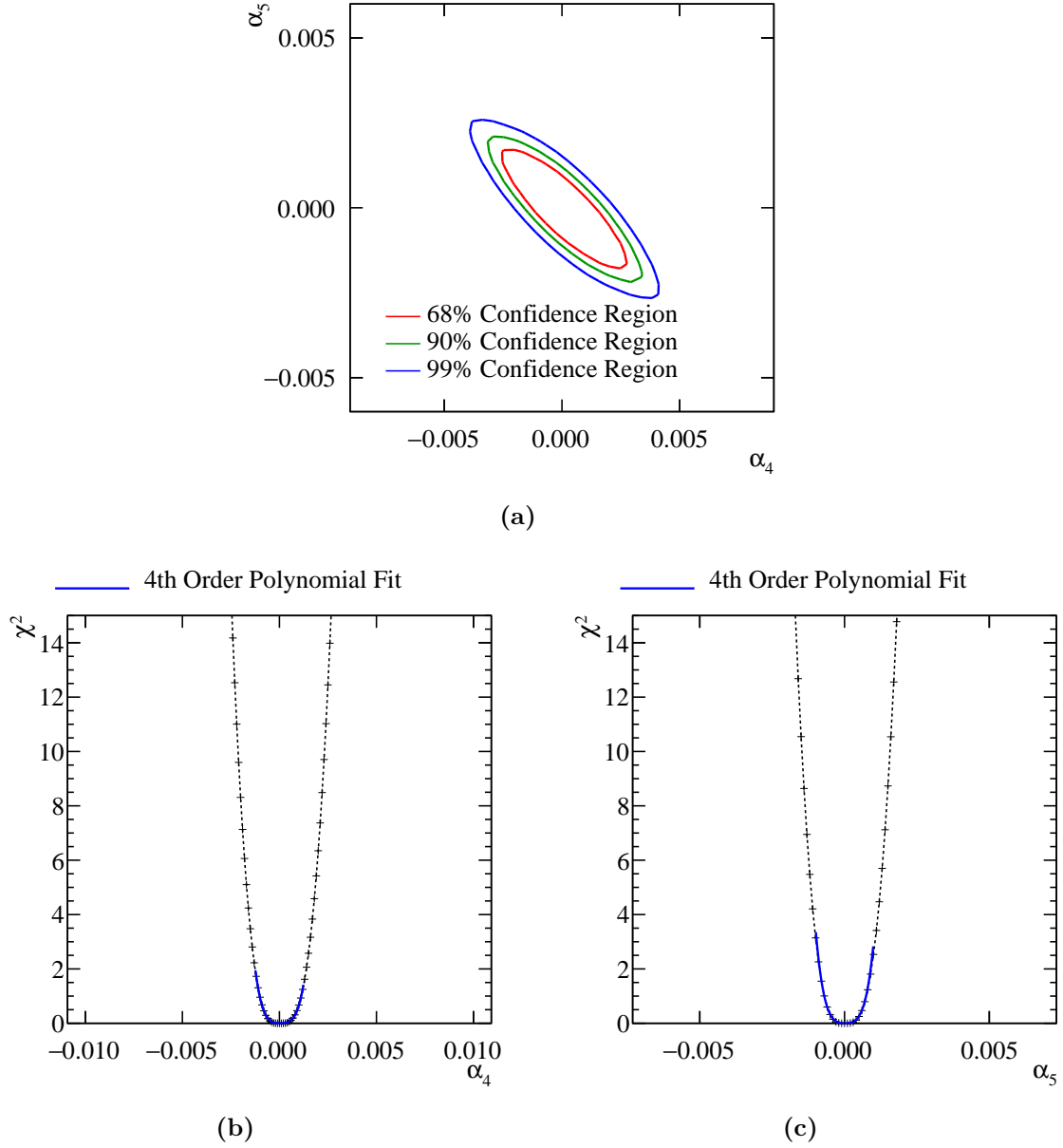
Figure 2.19: χ^2 sensitivity distributions from a fit to M_{VV} for $\sqrt{s} = 3$ TeV. Results include the effect of backgrounds after the application of a series of preselection cuts and MVA. (a) χ^2 sensitivity contours in α_4 and α_5 space. (b) χ^2 as a function of α_4 assuming $\alpha_5 = 0$. (c) χ^2 as a function of α_5 assuming $\alpha_4 = 0$.

(a)   (b)
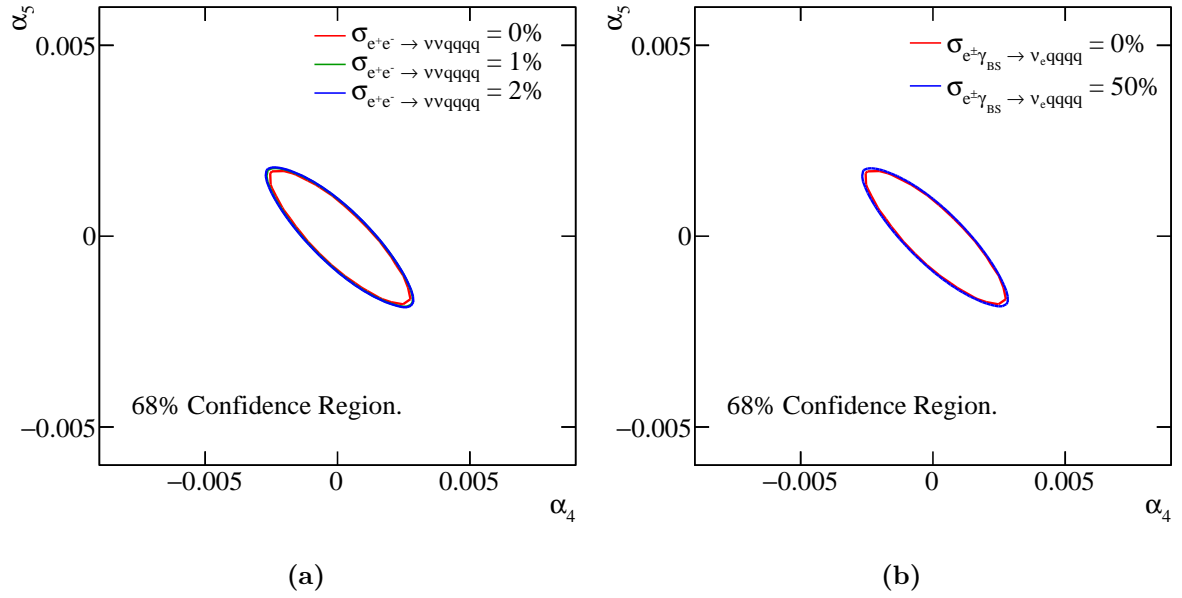
Figure 2.20: The 68% confidence region including the effect of uncertainties in the cross-section
for (a) the signal process $e^+e^- \to \nu\nu qqqq$ and (b) the dominant background
processes $e^{\pm}\gamma_{BS} \to \nu_e qqqq$.

Colophon

This thesis was made in LaTeX 2ε using the "hepthesis" class [30].

Bibliography

[1] Halina Abramowicz et al. The International Linear Collider Technical Design Report - Volume 4: Detectors. 2013.

[2] Lucie Linssen, Akiya Miyamoto, Marcel Stanitzki, and Harry Weerts. Physics and Detectors at CLIC: CLIC Conceptual Design Report. 2012.

[3] C. W. Fabjan and F. Gianotti. Calorimetry for particle physics. *Rev. Mod. Phys.*, 75:1243–1286, 2003.

[4] M. A. Thomson. Particle Flow Calorimetry and the PandoraPFA Algorithm. *Nucl. Instrum. Meth.*, A611:25–40, 2009.

[5] M. Derrick, D. Gacek, N. Hill, B. Musgrave, R. Noland, E. Petereit, J. Repond, R. Stanek, and K. Sugano. Design and construction of the ZEUS barrel calorimeter. *Nucl. Instrum. Meth.*, A309:77–100, 1991.

[6] Huong Lan Tran, Katja Krüger, Felix Sefkow, Steven Green, John Marshall, Mark Thomson, and Frank Simon. Software compensation in Particle Flow reconstruction. 2017.

[7] R. Wigmans. Calorimetry: Energy measurement in particle physics. *Int. Ser. Monogr. Phys.*, 107:1–726, 2000.

[8] L. Landau. On the energy loss of fast particles by ionization. *J. Phys.(USSR)*, 8:201–205, 1944.

[9] H. Bichsel, Donald E. Groom, and S. R. Klein. Passage of particles through matter. 2004.

[10] Oskar Hartbrich. AHCAL Digitisation. CALICE Spring Meeting 2015 & LCWS 2015, Tsukuba (Japan), 19 Apr 2015 - 24 Apr 2015, Apr 2015.

[11] C. Adloff et al. Hadronic energy resolution of a highly granular scintillator-steel

hadron calorimeter using software compensation techniques. *JINST*, 7:P09017, 2012.

[12] C. Adloff et al. The Time Structure of Hadronic Showers in highly granular Calorimeters with Tungsten and Steel Absorbers. *JINST*, 9:P07022, 2014.

[13] E. Fermi. An attempt of a theory of beta radiation. 1. *Z. Phys.*, 88:161–177, 1934.

[14] Georges Aad et al. Evidence for Electroweak Production of $W^{\pm}W^{\pm}jj$ in pp Collisions at $\sqrt{s} = 8$ TeV with the ATLAS Detector. *Phys. Rev. Lett.*, 113(14):141803, 2014.

[15] J. Beringer et al. Review of Particle Physics (RPP). *Phys. Rev.*, D86:010001, 2012.

[16] Wolfgang Kilian, Thorsten Ohl, and Jurgen Reuter. WHIZARD: Simulating Multi-Particle Processes at LHC and ILC. *Eur. Phys. J.*, C71:1742, 2011.

[17] Mauro Moretti, Thorsten Ohl, and Jurgen Reuter. O'Mega: An Optimizing matrix element generator. 2001.

[18] Torbjorn Sjostrand, Stephen Mrenna, and Peter Z. Skands. PYTHIA 6.4 Physics and Manual. *JHEP*, 05:026, 2006.

[19] G. Alexander et al. A Comparison of b and u d s quark jets to gluon jets. *Z. Phys.*, C69:543–560, 1996.

[20] Z. Was. TAUOLA the library for tau lepton decay, and KKMC / KORALB / KORALZ /... status report. *Nucl. Phys. Proc. Suppl.*, 98:96–102, 2001. [,96(2000)].

[21] Toshinori Abe et al. The International Large Detector: Letter of Intent. 2010.

[22] P. Mora de Freitas and H. Videau. Detector simulation with MOKKA / GEANT4: Present and future. In *Linear colliders. Proceedings, International Workshop on physics and experiments with future electron-positron linear colliders, LCWS 2002, Seogwipo, Jeju Island, Korea, August 26-30, 2002*, pages 623–627, 2002.

[23] S. Agostinelli et al. GEANT4: A Simulation toolkit. *Nucl. Instrum. Meth.*, A506:250–303, 2003.

[24] F. Gaede. Marlin and LCCD: Software tools for the ILC. *Nucl. Instrum. Meth.*, A559:177–180, 2006.

[25] J. S. Marshall, A. Münnich, and M. A. Thomson. Performance of Particle Flow Calorimetry at CLIC. *Nucl. Instrum. Meth.*, A700:153–162, 2013.

[26] W. Kilian. WHIZARD 1.0: A generic Monte-Carlo integration and event generation package for multi-particle processes.

[27] Matteo Cacciari, Gavin P. Salam, and Gregory Soyez. FastJet User Manual. *Eur. Phys. J.*, C72:1896, 2012.

[28] O. Wendt, F. Gaede, and T. Kramer. Event Reconstruction with MarlinReco at the ILC. *Pramana*, 69:1109–1114, 2007.

[29] Andreas Hoecker, Peter Speckmayer, Joerg Stelzer, Jan Therhaag, Eckhard von Toerne, and Helge Voss. TMVA: Toolkit for Multivariate Data Analysis. *PoS*, ACAT:040, 2007.

[30] Andy Buckley. The hepthesis LaTeX class.